PNAS RESEARCH ARTICLE | NEUROSCIENCE OPEN ACCESS

Hedgehog-interacting protein acts in the habenula to regulate nicotine intake

Stephanie P. B. Caligiuri[a], William M. Howe[a,1], Lauren Wills[a], Alexander C. W. Smith[a], Ye Lei[a], Purva Bali[a], Mary P. Heyer[a], Janna K. Moen[a], Jessica L. Ables[a], Karim S. Elayouby[a], Maya Williams[a], Clementine Fillinger[a], Zainab Oketokoun[a], Vanessa E. Lehmann[a], Alexandra G. DiFeliceantonio[a,2], Paul M. Johnson[b], Kristin Beaumont[c], Robert P. Sebra[c], Ines Ibanez-Tallon[d], and Paul J. Kenny[a,3]

Edited by Susan Amara, NIH, Bethesda, MD; received June 8, 2022; accepted August 28, 2022

Hedgehog-interacting protein (HHIP) sequesters Hedgehog ligands to repress Smoothened (SMO)-mediated recruitment of the GLI family of transcription factors. Allelic variation in HHIP confers risk of chronic obstructive pulmonary disease and other smoking-related lung diseases, but underlying mechanisms are unclear. Using single-cell and cell-type-specific translational profiling, we show that HHIP expression is highly enriched in medial habenula (MHb) neurons, particularly MHb cholinergic neurons that regulate aversive behavioral responses to nicotine. HHIP deficiency dysregulated the expression of genes involved in cholinergic signaling in the MHb and disrupted the function of nicotinic acetylcholine receptors (nAChRs) through a PTCH-1/cholesterol-dependent mechanism. Further, CRISPR/Cas9-mediated genomic cleavage of the *Hhip* gene in MHb neurons enhanced the motivational properties of nicotine in mice. These findings suggest that HHIP influences vulnerability to smoking-related lung diseases in part by regulating the actions of nicotine on habenular aversion circuits.

nicotine | habenula | single-cell RNA sequencing | hedgehog signaling | chronic obstructive pulmonary disease

Significance

Allelic variation in HHIP confers risk of smoking-related lung disease. We show that HHIP is expressed in the medial habenula, where it regulates the motivational properties of nicotine. These findings have relevance for understanding habenular involvement in nicotine aversion and mechanisms of genetic vulnerability to smoking-related diseases.

Habitual tobacco use is a leading cause of diseases of the respiratory system, including chronic obstructive pulmonary disease (COPD) and lung cancer (1, 2). Nicotine is the major reward-enhancing component of tobacco responsible for establishing and maintaining the smoking habit (3). Nicotine also has aversive properties that promote avoidance of tobacco products (4). Stronger aversive reactions to nicotine decrease the likelihood of progressing from occasional to habitual tobacco use (4, 5), whereas gene variants that attenuate nicotine aversion are associated with comparatively high levels of tobacco use and increased risk of COPD and other smoking-related diseases (6–10). Neuronal nicotinic acetylcholine receptors (nAChRs) regulate the actions of nicotine in the brain (11). Medial habenula (MHb) neurons, which project exclusively to the interpeduncular nucleus (IPn) via the fasciculus retroflexus (12, 13), express some of the highest concentrations of nAChRs in the brain (14). Disruption of nAChR-mediated transmission in the MHb or IPn attenuates nicotine aversion and increases nicotine intake in rats and mice (15–18). Conversely, manipulations that enhance the stimulatory effects of nicotine on the MHb–IPn circuit amplify nicotine aversion and decrease nicotine intake (19–21). Thus, the MHb–IPn circuit is thought to regulate the "set point" of nicotine aversion to influence vulnerability to tobacco dependence and smoking-related diseases (4). Molecular and cellular processes in the MHb–IPn circuit that regulate nicotine consumption remain poorly characterized.

The Hedgehog signaling pathway is a core regulator of tissue patterning during embryonic development and tissue homeostasis and repair in adulthood (22, 23). Patched-1 (PTCH-1) is the cognate transmembrane receptor for Hedgehog ligands (24–27) and functions to transport cholesterol and other oxysterols away from regions of the plasma membrane where they are required for Smoothened (SMO) activity (28–31). Binding of hedgehog ligands to PTCH-1 triggers its internalization, which permits cholesterol to accumulate to levels sufficient to activate SMO (29–32). Activated SMO then recruits members of the glioma-associated oncogene homolog (GLI) family of zinc-finger transcription factors to drive Hedgehog-responsive gene expression (33). Hedgehog-interacting protein (HHIP) is an endogenous inhibitor of Hedgehog signaling that sequesters Hedgehog ligands to facilitate PTCH-1 activity (34–36). Genetic variation in a region of chromosome 4q31 that contains an enhancer element for the *HHIP* gene (37) decreases HHIP expression in lung tissue and elevates risk of COPD (6, 37–40) and other smoking-related lung diseases (10, 41). *Hhip* homozygous ($Hhip^{-/-}$) mutant mice die during the early postnatal period due to respiratory failure secondary to abnormalities in lung development (34, 42). *Hhip* heterozygous ($Hhip^{+/-}$) mutant mice, which survive into adulthood, demonstrate spontaneous age-related deficits in lung function that resemble COPD (43).

Author affiliations: [a]Nash Family Department of Neuroscience, Icahn School of Medicine at Mount Sinai, New York, NY 10029; [b]Department of Information Technology and Electrical Engineering, ETH Zürich, 8092 Zürich, Switzerland; [c]Department of Genetics and Genomic Sciences, Icahn School of Medicine at Mount Sinai, New York, NY 10029; and [d]Laboratory of Molecular Biology, The Rockefeller University, New York, NY 10065

Author contributions: S.P.B.C., P.N.J., I.I.T., and P.J.K. designed research; S.P.B.C., W.M.H., Y.L., P.B., M.P.H., J.K.M., J.L.A., K.S.E., M.W., C.F., Z.O., K.B., and R.P.S. performed research; S.P.B.C., L.W., A.C.W.S., V.E.L., A.G.D., I.I.T., and P.J.K. analyzed data; and S.P.B.C. and P.J.K. wrote the paper.

Competing interest statement: P.J.K. is cofounder of Eolas Therapeutics Inc., which has a licensing agreement with AstraZeneca to develop small-molecule treatments for substance use disorders.

This article is a PNAS Direct Submission.

Copyright © 2022 the Author(s). Published by PNAS. This open access article is distributed under Creative Commons Attribution-NonCommercial-NoDerivatives License 4.0 (CC BY-NC-ND).

[1]Present address: School of Neuroscience at the College of Science, Virginia Tech, Blacksburg, VA 24061.

[2]Present address: Department of Human Nutrition, Foods and Exercise, College of Agriculture and Life Sciences and Center for Transformative Research on Health Behaviors, Fralin Biomedical Research Institute, Virginia Tech, Blacksburg, VA 24061.

[3]To whom correspondence may be addressed. Email: paul.kenny@mssm.edu.

This article contains supporting information online at http://www.pnas.org/lookup/suppl/doi:10.1073/pnas.2209870119/-/DCSupplemental.

Published November 8, 2022.

Furthermore, *HHIP* alleles confer risk of lung disease in humans regardless of smoking status (44, 45). Thus, HHIP involvement in smoking-related respiratory diseases is generally attributed to its important roles in the development, maintenance, and repair of lung tissue (38, 46). Here, we report that HHIP interacts with PTCH-1 to regulate nAChR function by controlling local cholesterol gradients in plasma membranes. We show that HHIP is densely expressed in the habenula, particularly by MHb cholinergic neurons, where it regulates the motivational properties of nicotine. These findings reveal a role for HHIP in regulating cholinergic signaling in the MHb–IPn circuit and suggest that HHIP alleles influence risk of smoking-related lung diseases in part by regulating the actions of nicotine on habenular aversion circuits.

Results

Single-Cell RNA Sequencing Identifies Nicotine-Responsive Cells in Habenula. The habenula is segregated into medial (MHb) and lateral (LHb) compartments that are anatomically, transcriptionally, and functionally distinct (12, 13). Nicotine stimulates MHb and LHb neurons in ex vivo slice preparations (18, 47–49), actions thought to contribute to nicotine aversion (50). However, the in vivo effects of nicotine on habenular activity are poorly characterized. Thus, we delivered an adeno-associated virus that expressed GCaMP6m in a Cre-dependent manner (AAV-FLEX-GCaMP6m) into the habenula of *Gpr151-Cre* mice and used fiber photometry to monitor nicotine-induced changes in habenular activity in freely moving mice (Fig. 1*A*). In *Gpr151-Cre* mice, the majority of Cre-mediated recombination events occur in choline *O*-acetyltransferase–expressing cholinergic neurons in ventral domains of MHb (MHb^{Chat} neurons) (51, 52), with sparse recombination also occurring in substance P-containing neurons in dorsal MHb and *Chrm2*-expressing neurons in LHb (51, 52). At least 3 wk after GCaMP6m infusion, mice were subcutaneously (SC) injected with saline or a dose of nicotine (1 $mg{\cdot}kg^{-1}$) equivalent to amounts volitionally consumed by mice during daily (60 min) intravenous nicotine self-administration sessions (15, 20). We detected increases in GCaMP-derived fluorescence after nicotine but not saline injection (Fig. 1 *B* and *C*), confirming that nicotine stimulates habenular activity in vivo similar to its effects in slice preparations.

Next, we used single-cell RNA sequencing (scRNA-seq) to identify cell populations in the habenula that demonstrate transcriptional responses to nicotine. We injected C57BL6/J mice with the same dose of nicotine (1 $mg{\cdot}kg^{-1}$) that stimulated an increase in habenular activity in *Gpr151-Cre* mice for three consecutive days and collected habenular tissue for scRNA-Seq. 24 h after the final injection. Sequencing was performed using the 10x Genomics Chromium and Illumina NovaSEq. 6000 platforms, with reads mapped to a reference genome using CellRanger from 10x Genomics, and transcriptomes clustered using the Scanpy toolkit (53) (*Materials and Methods*) (Fig. 1*D*). After filtering for quality control, the transcriptomes of 9,946 cells from saline- and nicotine-treated mice were analyzed (*SI Appendix*, Supplementary Table 1). Compared with saline-treated mice, cells from nicotine-treated mice contained higher concentrations of mitochondrial gene transcripts and lower mean reads per cell and demonstrated other features reflective of poor health (*SI Appendix*, Supplementary Table 1). This is consistent with reports suggesting that habenular neurons, particularly MHb^{Chat} neurons, are remarkably sensitive to nicotine-induced excitotoxicity and cell death (54, 55). Consequently, only ~25% of the cells that passed quality control and were included in analyses were derived from nicotine-treated mice (Fig. 1*E*). Cells from saline- and nicotine-treated mice distributed into 11 discrete clusters in Uniform Manifold Approximation and Projection (UMAP) space (Fig. 1 *D* and *E*). Clusters 0 (3,395 cells), 5 (696 cells), and 11 (149 cells) contained gene transcripts known to be expressed by habenular neurons, including *Thy1* and *Syt1* (56, 57) (Fig. 1*F*). Cells with genetic profiles consistent with MHb neurons were contained in clusters 0 and 5 (Fig. 1*G*), with *Chat*-expressing cholinergic neurons concentrated in cluster 0 (Fig. 1*G* and *SI Appendix*, Fig. S1). Cells expressing features consistent with LHb neurons were concentrated in cluster 0 (Fig. 1*H*). Neurons in clusters 0 and 5, but not in cluster 11, were transcriptionally responsive to nicotine (Fig. 1*I*; *SI Appendix*, Supplementary Tables 2–4). Kyoto Encyclopedia of Genes and Genomes (KEGG) analysis of differentially expressed genes (DEGs) in cluster 0 suggested that pathways involved in extracellular matrix remodeling, neuroplasticity-related events, and transforming growth factor β (TGF-β) signaling were modified by nicotine (Fig. 1*J*). KEGG analysis of DEGs in cluster 5 suggested that signaling processes involved in cholinergic transmission and nicotine addiction were impacted by nicotine (Fig. 1*K*). Upstream regulator analysis revealed that many of the DEGs in clusters 0 and 5 were regulated by TGF-β and/or insulin-like growth factor 1 (IGF1) signaling (*SI Appendix*, Fig. S2). This is notable because TGF-β and IGF1 signaling are coordinated by primary cilia (58) and the MHb is known to be highly enriched in cilia-associated genes (59). Thus, nicotine modifies gene expression in MHb and LHb neurons, with cilium-related signaling pathways likely to play an important role in transducing these responses in MHb neurons.

Cholinergic Neurons in Habenula Express Genes Linked to Smoking-Associated Diseases. MHb^{Chat} neurons are highly sensitive to the stimulatory effects of nicotine in slice preparations (48) and undergo functional adaptations in response to chronic nicotine exposure that contribute to the development of nicotine dependence (48, 60–62). Besides nAChRs (15–18), little is known about the genes expressed by MHb^{Chat} neurons that regulate their responsiveness to nicotine (19). Translating ribosome affinity purification-sequencing (TRAP-seq) enables cell-type-specific RNA sequencing at much greater read depths than current scRNA-seq technologies, with the added advantage that transcripts undergoing active translation into their protein products can be identified (Fig. 2*A*). Thus, we used TRAP-seq to identify genes expressed by MHb^{Chat} neurons that may regulate behavioral responses to nicotine. Habenula tissue was collected from $Chat^{DW167}$ *TRAP* mice, in which the L10a ribosomal subunit tagged with enhanced green fluorescent protein (eGFP) is expressed by MHb^{Chat} neurons (63). After RNA–protein cross-linking, L10a-eGFP–associated RNAs were immunoprecipitated from the habenula and sequenced using the Illumina HiSeq 2500 instrument (Fig. 2*A*). Immunoprecipitated gene transcripts were rank-ordered according to their relative abundance in L10a-containing ribosomal complexes, with the top 1,000 translated genes prioritized for further assessment (*SI Appendix*, Supplementary Table 5). Prioritized genes were screened against all published human genome-wide association studies using the "GWAS Catalog" feature in Enrichr (64) (Fig. 2*A*). This analysis revealed that 61 of the most abundantly translated genes in MHb^{Chat} neurons are associated with genetic vulnerability to smoking-related behaviors and/or diseases (Fig. 2*B*). Assessment of the Allen Brain Atlas suggested that many of these 61 genes are transcribed at higher levels in the MHb than other brain regions (Fig. 2*B* and *SI Appendix*, Fig. S3). These genes included the nAChR subunit genes *CHRNA3*, *CHRNB3*, and *CHRNB4* (Fig. 2*B*), which contain well-established genetic risk factors for tobacco dependence and smoking-related diseases (Fig. 2*B*). This analysis also identified habenula-enriched genes associated with

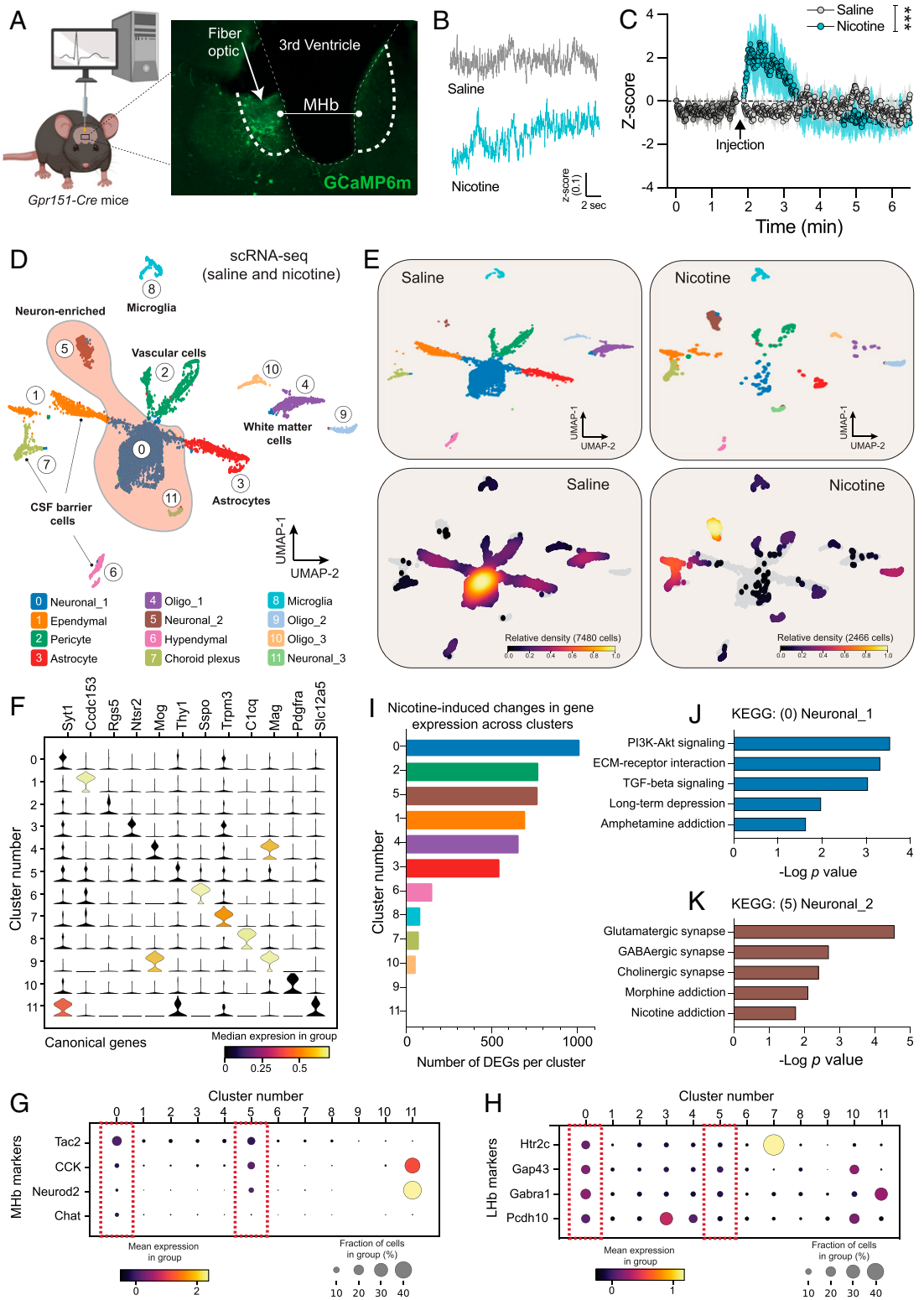

Fig. 1. Identification of nicotine-responsive cells in habenula. (*A*) Fiber photometry was used to monitor neural activity in the habenula of *Gpr151-Cre* mice (n = 5 mice). Shown is a representative example of habenular GCaMP6m expression. (*B*) Representative photometry traces after saline and nicotine (1 mg·kg^{-1} SC) injection. (*C*) Nicotine, but not saline, injection elevated GCaMP-mediated fluorescence in habenula (mean z-score ± SEM); $F_{(469,\ 3283)} = 4.276$, ***$P < 0.0001$, interaction effect between nicotine and time in two-way repeated-measures ANOVA. (*D*) scRNA-seq was performed on habenula tissue from saline- and nicotine-injected mice (n = 6 mice per group). Shown is a UMAP dimensionality reduction plot of cell clustering based on expression profiles. (*E*) UMAPs of cell clusters from saline- and nicotine-treated mice based on expression profiles (*Upper*) and cell densities across clusters (*Lower*). (*F*) Violin plot of expression of cell-type-specific canonical genes across cell clusters. (*G*) Dot plot of gene transcripts that identify MHb neurons. Red boxes indicate cell clusters enriched in MHb neuron marker genes. (*H*) Dot plot of gene transcripts that identify LHb neurons. Red boxes indicate cell clusters enriched in LHb neuron marker genes. (*I*) Numbers of DEGs ($P < 0.05$ in each case; Fisher's exact test between saline- and nicotine-treated mice) across cell clusters. (*J*) KEGG analysis of DEGs in cluster 0 cells (−log P value; Fisher's exact test). (*K*) KEGG analysis of DEGs in cluster 5 (−log P value; Fisher's exact test).

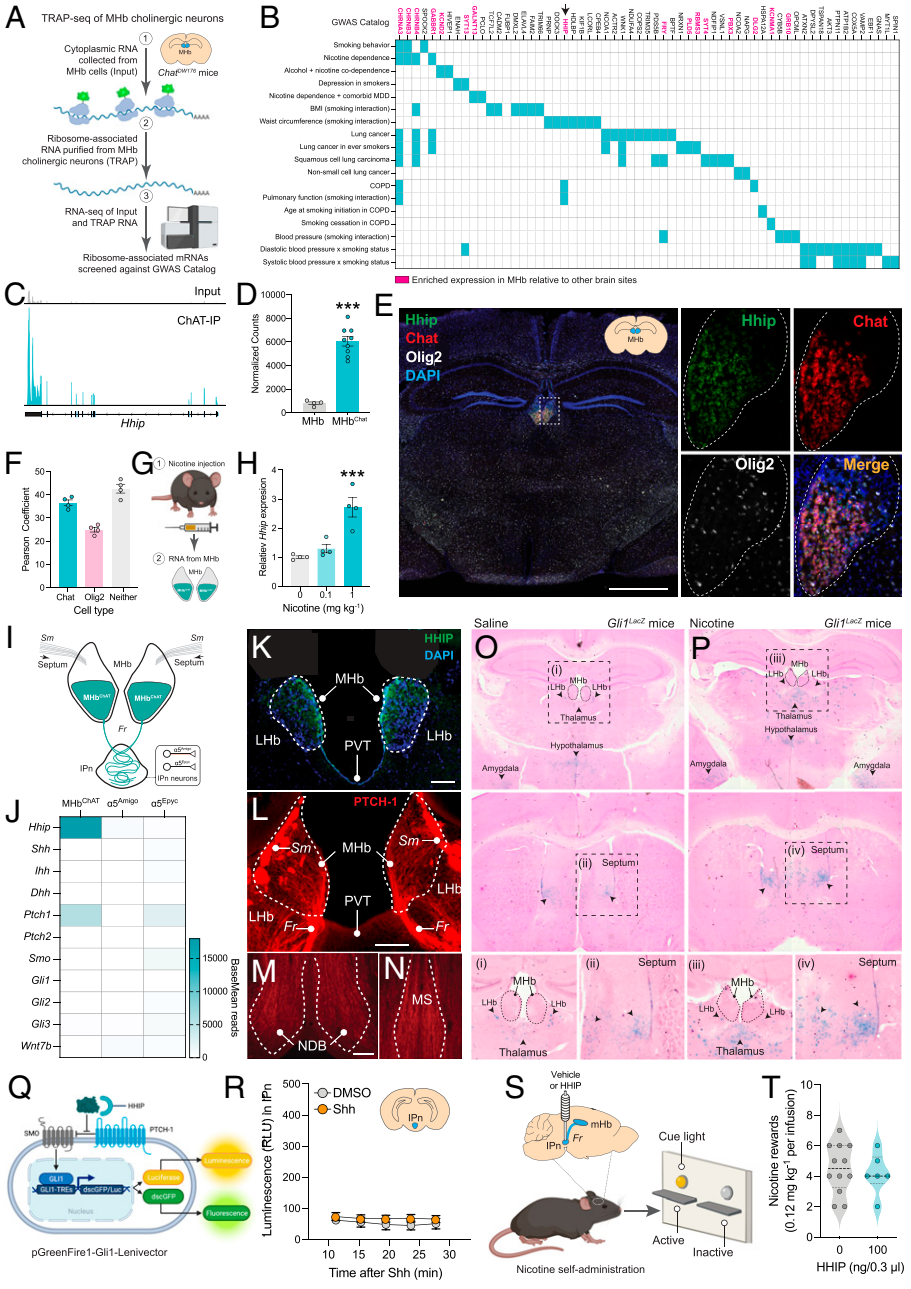

Fig. 2. HHIP is expressed by habenular cholinergic neurons. (*A*) Graphical representation of TRAP-seq procedure to identify L10a-associated mRNAs undergoing translation in MHb^{Chat} neurons using *ChAT*^{DW167} mice, which were screened against GWAS Catalog using Enrichr. (*B*) Sixty-one of the most abundantly translated genes in MHb^{Chat} neurons are associated with increased risk of smoking-related behaviors or disease. Genes in pink are expressed more densely in MHb relative to other brain regions. (*C*) Representative RNA-seq reads of L10a-associated transcripts in MHb^{Chat} neurons aligned to *Hhip* gene (*Left*). (*D*) Relative *Hhip* reads (mean ± SEM) in MHb^{Chat} neurons from TRAP-seq of *ChAT*^{DW167} mice (n = 9) and in MHb tissue from RNA-seq of habenula tissue from wild-type mice (MHb; n = 6); ***P < 0.001, unpaired two-sided t test. (*E*, *Left*) Coronal brain slice from C57BL6J mouse showing RNAscope in situ hybridization of *Hhip*, *Chat*, and *Olig2* transcripts, with right hemisphere MHb identified by white box. (*E*, *Right*) High-magnification images of the same right hemisphere of MHb identified by white demarcation lines. (*F*) Pearson coefficient of *Hhip* expression in cells that coexpressed *Chat*, *Olig2*, or neither of these transcripts. (*G*) Graphical representation of experimental procedure to investigate the effect of acute nicotine injection (1 mg·kg^{-1} SC) on habenular HHIP expression. (*H*) Normalized *Hhip* expression in MHb of mice injected with saline or nicotine (n = 6 per group); main effect of nicotine in one-way ANOVA: $F_{(2,\ 9)}$ = 19.12, P = 0.0006; ***P = 0.007 compared with saline-treated mice, Tukey multiple comparison test. (*I*) Graphical representation of septal inputs to MHb–IPn circuit and the two major population of α5 nAChR-expressing neurons contained in IPn (α5^{Amigo} and α5^{Epyc} neurons). *Sm*, stria medullaris; *Fr*, fasciculus retroflexus. (*J*) Heat map of normalized TRAP-seq reads of Hedgehog pathway gene transcripts contained in MHb^{Chat}, α5^{Amigo}, or α5^{Epyc} neurons. Shh, sonic hedgehog; Ihh, Indian hedgehog; Dhh, desert hedgehog; Wnt7b, wingless-type MMTV integration site family, member 7b. (*K*) Fluorescence micrograph of HHIP protein expression (green) in MHb of mice. Cell nuclei are highlighted by DAPI staining (blue). (Scale bar: 100 µM.) (*L*) Micrograph of PTCH-1 protein expression (red) in MHb of mice. PVT, paraventricular nucleus of thalamus. (Scale bar: 100 µM.) (*M*) Immunofluorescent images of PTCH-1 protein expression in NDB: Nucleus of the Diagonal Band. (Scale bar: 100 µM.) (*N*) PTCH-1 in MS: Medial Septum. (*O* and *P*) Whole-brain slides identifying GLI1-driven β-gal activity (blue stain; identified by black arrows) in adult *Gli1*^{LacZ} reporter mice injected with saline (*O*) or nicotine (1 mg·kg^{-1} per) (*P*) on three consecutive days and assessed 24 h after final injection. Areas of MHb and septum in boxes (i and ii, respectively) from saline- and nicotine-treated mice are shown in higher magnification in bottom panels. (*Q*) Graphical representation of GLI1 lentireporter. (*R*) GLI-driven luciferase activity in ex vivo brain slices of rats expressing the GLI-lentireporter in IPn and treated with vehicle (n = 4) or recombinant Shh protein (n = 9). Main effect of Shh protein: $F_{(1,\ 11)}$ = 0.6668, P = 0.4315; main effect of time: $F_{(2.917,\ 32.09)}$ = 1.935, P = 0.1451; interaction effect: $F_{(4,\ 44)}$ = 0.5448, P = 0.7037. (*S*) Graphical representation of IPn cannulation and injection of recombinant HHIP protein (100 ng) into the IPn of nicotine self-administering rats. (*T*) Number of nicotine rewards (0.12 mg·kg^{-1} per infusion) earned by rats after intra-IPn injection of vehicle (n = 12) or HHIP (n = 6); P = 0.6704, unpaired two-sided t test.

smoking-related diseases but not previously investigated in the context of behavioral responses to nicotine (Fig. 2*B*). Notable among these genes was *HHIP*, which is associated with risk of COPD and poor lung function in individuals who smoke (6, 37–40) (Fig. 2 *B* and *C* and *SI Appendix*, Fig. S3). Approximately sixfold higher concentrations of *Hhip* transcripts were detected in ribosomal complexes in MHb^{Chat} neurons compared with concentrations detecting using bulk RNA-seq of habenular tissue from a separate cohort of wild-type mice (Fig. 2*D*). This suggests that HHIP is translated at high levels by MHb^{Chat} neurons relative to other cell types in the habenula. RNAscope fluorescence in situ hybridization confirmed that HHIP expression was much higher in the MHb than surrounding brain regions (Fig. 2*E* and *SI Appendix*, Fig. S4). HHIP was also expressed by cells in the fasciola cinerea region of the hippocampus and in sparsely distributed cells throughout the striatum, where HHIP is known to be expressed by nitric oxide synthase–containing interneurons (65) (Fig. 2*E* and *SI Appendix*, Fig. S4). In the MHb, *Hhip* transcripts were detected in ∼35% of cells that expressed *Chat* (Fig. 2 *E* and *F* and *SI Appendix*, Fig. S4), in ∼25% of *Olig2*-expressing oligodendrocytes, and in ∼40% of cells that expressed neither *Chat* nor *Olig2* (Fig. 2 *E* and *F*) but enriched in the neuronal marker gene *Slc17a6* (*SI Appendix*, Fig. 4). scRNA-seq data from saline- and nicotine-treated mice (see Fig. 1) suggested that HHIP expression was unaltered by nicotine in any cell cluster when expression was assessed 24 h after the final injection (*SI Appendix*, Supplementary Tables 3 and 4). However,

habenular HHIP expression was up-regulated by nicotine (1 mg·kg^{-1}) in mice when expression was assessed 90 min after injection (Fig. 2 *G* and *H*). These findings demonstrate that HHIP is densely expressed by neurons in the MHb, particularly MHb cholinergic neurons, where its expression is transiently (<24 h) increased by nicotine treatment.

SMO/GLI-Mediated Hedgehog Signaling Is Quiescent in Adult MHb Neurons. HHIP is synthesized by Hedgehog-responsive cells to sequester Hedgehog ligands and provide negative feedback onto Hedgehog signaling pathways (34). MHb^{Chat} neurons receive synaptic input almost exclusively from regions of the septum in which neurons synthesize and secrete Hedgehog ligands (66, 67) (Fig. 2*I*). Thus, we hypothesized that HHIP is produced by MHb neurons to regulate Hedgehog signaling driven by septal afferents. To test this hypothesis, we first inspected the TRAP-seq data from *Chat*^{DW167} mice to determine whether other core components of the Hedgehog signaling pathway were expressed by MHb^{Chat} neurons. High concentrations of *Ptch1* transcripts, which encode the cognate receptor for Hedgehog ligands (PTCH-1), were detected in ribosomal complexes from MHb^{Chat} neurons (Fig. 2*J*). Consistent with the TRAP-seq data, HHIP and PTCH-1 protein expression was detected in the MHb of mice via immunofluorescence (Fig. 2 *K* and *L*). PTCH-1–expressing fibers were also detected in the nucleus of the diagonal band (NDB) and medial septum (MS) (Fig. 2 *M* and *N*), which project to the MHb via the stria medullaris (Fig. 2*I*). Surprisingly, SMO, members of the GLI family of transcription factors, and Sonic (Shh), Indian (Ihh), or Desert (Dhh) Hedgehog ligands and other core components of the Hedgehog signaling pathway were translated at very low or undetectable levels by MHb^{Chat} neurons (Fig. 2*J*). Analysis of scRNA-seq data from saline-treated mice (see Fig. 1) similarly showed that SMO and GLI transcription factors were expressed at near-undetectable levels by MHb neurons in the habenula but were sparsely expressed by habenular astrocytes and ependymal cells (*SI Appendix*, Fig. S5). Predicted upstream transcriptional regulators of the 1,000 most abundantly translated genes in MHb^{Chat} neurons identified by TRAP-seq (*SI Appendix*, Supplementary Table 6) suggested that their expression was regulated by POU4F1, NEUROD1, CREB, and other transcription factors known to be expressed by MHb neurons, but not by GLI transcription factors (*SI Appendix*, Fig. S6). Next, we used *Gli1*^{LacZ} reporter mice injected with saline or nicotine (1 mg·kg^{-1} per day for 3 d) to assess brain-wide patterns of GLI1-mediated transcriptional activity under baseline and nicotine-treatment conditions, as reflected by β-galactosidase (β-gal) activity (66). GLI-driven β-gal activity was detected in the NDB and MS regions of the septum, dorsal thalamus, hypothalamus, and the amygdala of saline- and nicotine-treated *Gli1*^{LacZ} mice (Fig. 2 *O* and *P*). β-gal activity was also detected in the LHb (Fig. 2 *O* and *P*), likely reflecting Hedgehog signaling in LHb astrocytes (*SI Appendix*, Fig. S5). However, GLI1-driven β-gal activity was not detected in the MHb of saline- or nicotine-treated *Gli1*^{LacZ} reporter mice (Fig. 2 *O* and *P*). Combined, these findings suggest that SMO/GLI-mediated canonical Hedgehog signaling is quiescent in MHb cholinergic (and noncholinergic) neurons even though they express high concentrations of HHIP and PTCH-1.

MHb^{Chat} neurons project exclusively to the IPn, where acetylcholine released by these cells modulates IPn neurons via α5 subunit-containing (α5*) nAChRs (60) (Fig. 2*I*). It is possible that HHIP is also secreted by MHb^{Chat} neurons into the IPn, where it modulates Hedgehog signaling in IPn neurons. There are two major populations of α5* nAChR-expressing neurons in the IPn (60). The first expresses *Amigo1* (α5^{Amigo} neurons) and provides long-range projections to the raphe nuclei and other caudal brain sites (60) (Fig. 2*I*). The second expresses *Epyc* (α5^{Epyc} neurons) and likely serves as local interneurons along the IPn–raphe axis (60) (Fig. 2*I*). Inspection of previously collected TRAP-seq data from α5^{Amigo} and α5^{Epyc} neurons (60) showed that relatively high concentrations of *Ptch1* transcripts were associated with L10a-containing ribosomal complexes in α5^{Epyc} neurons (Fig. 2*J*). By contrast, HHIP, Hedgehog ligands, SMO, and GLI transcription factors were translated at very low or undetectable levels in α5^{Amigo} and α5^{Epyc} IPn neurons (Fig. 2*J*). GLI-mediated transcriptional activity was not detected in the IPn of saline- or nicotine-treated *Gli1*^{LacZ} reporter mice (not shown). Similarly, baseline GLI-mediated transcriptional activity was at background levels in the IPn and was not enhanced by recombinant Shh protein, in ex vivo brain slices from rats expressing a GLI-luciferase reporter in the IPn (19) (Fig. 2 *Q* and *R*). Finally, recombinant HHIP protein injected directly into the IPn of rats had no effect on nicotine self-administration behavior (Fig. 2 *S* and *T*). Rats instead of mice were used for this experiment to facilitate accurate infusion of recombinant HHIP protein into the IPn. Together, these data suggest that Shh and other Hedgehog ligands are unlikely to stimulate canonical Hedgehog signaling in IPn neurons and that HHIP-regulated Hedgehog signaling in the IPn is unlikely to influence the motivational properties of nicotine.

HHIP Regulates Neuroplasticity-Related Gene Programs in MHb Neurons. The dense expression of HHIP and PTCH-1 by MHb^{Chat} neurons in the absence of core intracellular components of the Hedgehog signaling pathway could be a vestigial feature of these cells without any functional consequence. Alternatively, HHIP and PTCH-1 expressed on the surface of MHb^{Chat} neurons could signal through SMO/GLI-independent noncanonical mechanisms to modulate the activity of the MHb–IPn circuit. To investigate these possibilities, we performed scRNA-seq on habenular tissue collected from adult wild-type (*Hhip*$^{+/+}$) and HHIP haploinsufficient (*Hhip*$^{+/-}$) mice (43). After filtering for quality control, a total of 22,105 cells were included in the analyses (*SI Appendix*, Supplementary Table 7). Higher numbers of nonneuronal cells were collected from *Hhip*$^{+/-}$ mice compared with *Hhip*$^{+/+}$ mice, particularly astrocytes and microglia (*SI Appendix*, Fig. S6 and Supplementary Table 8), suggesting that HHIP exerts an inhibitory influence over the proliferation and/or maturation of habenular glial cells. Cells from *Hhip*$^{+/-}$ and *Hhip*$^{+/+}$ mice clustered into 11 distinct groups (Fig. 3*A* and *SI Appendix*, Supplementary Tables 9–11). Clusters 0, 5, and 10 demonstrated genetic features consistent with habenular neurons (56, 57), including expression of *Snap25* and *Syp* (Fig. 3*B*). Core marker genes of MHb neurons (e.g., *Tac2*) were expressed by cells in cluster 0 (*SI Appendix*, Fig. S7). Cluster 0 neurons also expressed genes involved in the synthesis and release of acetylcholine (*Chat* and *Slc18a3*) (Fig. 3*C*), suggesting that MHb^{Chat} neurons were contained within this cluster. Core marker genes of LHb neurons (e.g., *Pcdh10*) were expressed by cluster-10 cells (*SI Appendix*, Fig. S7). By contrast, cluster-5 cells contained relatively low levels of *Tac2* and *Pcdh10* transcripts but high concentrations of *Slc17a7* and *Gad1* transcripts (*SI Appendix*, Fig. S7). This profile is consistent with neurons located in the dorsal-most aspect of MHb at the interface of stria medullaris inputs (*SI Appendix*, Fig. S8), the function of which is currently unknown. HHIP

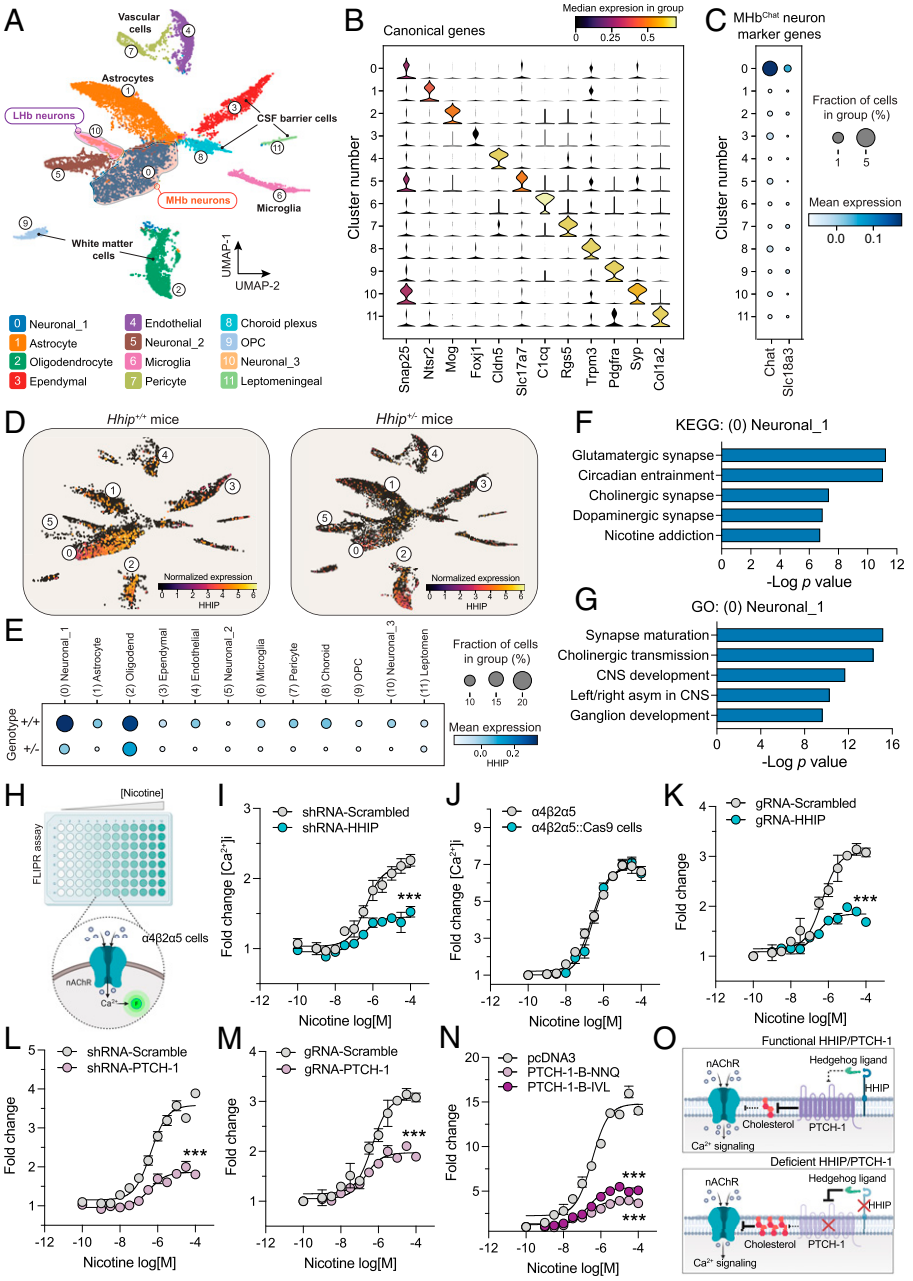

Fig. 3. HHIP regulates nAChR function. (*A*) UMAP dimensionality reduction plot of habenula cell clustering based on gene expression profiles from *Hhip*$^{+/+}$ and *Hhip*$^{+/-}$ mice (n = 6 per group). (*B*) Violin plot showing expression levels of cell-type-specific canonical genes across cell clusters. (*C*) Dot plot of gene transcripts used to identify putative MHb^{Chat} neurons across cell clusters. (*D*) UMAP plot showing relative HHIP expression across cell clusters in *Hhip*$^{+/+}$ and *Hhip*$^{+/-}$ mice. (*E*) Dot plot of *Hhip* transcript levels across cell clusters in *Hhip*$^{+/+}$ and *Hhip*$^{+/-}$ mice. (*F*) KEGG analysis of DEGs in putative habenula neurons contained in cluster 0 between *Hhip*$^{+/+}$ and *Hhip*$^{+/-}$ mice. (*G*) GO analysis (biological process) of DEGs in cluster 0. (*H*) Graphical representation of FLIPR intracellular calcium ([Ca^{2+}]i) assay to assess nAChR signaling in HEK 293 cells stably expressing α4β2α5 nAChRs. (*I*) Nicotine-stimulated increases in intracellular calcium [Ca^{2+}]i levels were attenuated by shRNA-mediated HHIP knockdown. Peak response for shRNA-Scrambled vs. shRNA-HHIP: $F_{(1,\ 138)}$ = 46.38, ***P < 0.0001; IC_{50} for shRNA-Scrambled vs. shRNA-HHIP: $F_{(1,\ 138)}$ = 0.750, P = 0.5413; curve fitting by nonlinear regression. (*J*) Stable expression of Cas9 in α4β2α5 nAChR HEK cells did not alter the potency or efficacy of nicotine-evoked increases in [Ca^{2+}]i. Peak response: $F_{(1,\ 66)}$ = 0.9362, P = 0.3368; IC_{50}: $F_{(1,\ 66)}$ = 1.317, P = 0.2552; curve fitting by nonlinear regression. (*K*) Nicotine-evoked [Ca^{2+}]i responses were attenuated by CRIPSR/Cas9-mediated genomic cleavage of *HHIP*. Peak response for sgRNA-Scrambled vs. sgRNA-HHIP: $F_{(1,\ 66)}$ = 79.10, ***P < 0.0001; IC_{50}: $F_{(1,66)}$ = 1.204, P < 0.2765; nonlinear regression. (L) Nicotine-evoked [Ca^{2+}]i responses were attenuated by shRNA-mediated PTCH-1 knockdown. Peak response: $F_{(1,306)}$ = 122.4, ***P < 0.0001; IC_{50}: $F_{(1,306)}$ = 0.2399, P = 0.6246; nonlinear regression. (*M*) Nicotine-evoked [Ca^{2+}]i responses were attenuated by CRIPSR/Cas9-mediated genomic cleavage of *PTCH1*. Peak response: $F_{(1,66)}$ = 100.9, ***P < 0.0001; IC_{50}: $F_{(1,66)}$ = 2.629, P = 0.1097; nonlinear regression. (*N*) Nicotine-evoked [Ca^{2+}]i responses were attenuated by expression of cholesterol transport-deficient PTCH-1 mutants (PTCH-1-B-NNQ and PTCH-1-B-IVL). Peak responses for pcDNA3 vs. PTCH-1-B-NNQ and pcDNA3 vs. PTCH-1-B-IVL were $F_{(1,\ 66)}$ = 53.29, ***P < 0.001 and $F_{(1,\ 66)}$ = 119.3, ***P < 0.001, respectively. IC_{50} comparisons for same groups were $F_{(1,66)}$ = 0.4919, P = 0.4855 and $F_{(1,66)}$ = 0.7424, P = 0.3920, respectively; nonlinear regression. (*O*) Graphical representation of proposed mechanism by which HHIP and PTCH-1 interact to control local plasma membrane cholesterol gradients and thereby regulate nAChR signaling.

expression was higher in the putative MHb neurons contained in cluster 0 than in any other cell cluster in *Hhip*$^{+/+}$ mice (Fig. 3 *D* and *E*) and these cells showed the greatest relative reduction in HHIP expression between *Hhip*$^{+/-}$ and *Hhip*$^{+/+}$ mice (Fig. 3 *D* and *E*). Notably, the relative reduction of HHIP transcripts in the putative oligodendrocytes contained in cluster 2 was much less than that observed in the MHb neurons contained in cluster 0 of HHIP haploinsufficient mice compared with wild-type mice (Fig. 3 *D* and *E*). The reason for this is unclear but could reflect a particularly important role of HHIP in regulating oligodendrocyte function in the MHb, which necessitated the greater engagement of compensatory mechanisms to maintain HHIP expression at near wild-type levels in the HHIP haploinsufficient mice. Cluster 0 MHb neurons had the highest number of DEGs of any cell cluster between *Hhip*$^{+/-}$ and *Hhip*$^{+/+}$ mice (*SI Appendix*, Fig. S9). Predicted upstream regulators of the DEGs in cluster-0 cells suggested that many were targets of TGF-β and IGF1 signaling (*SI Appendix*, Fig. S10), consistent with dysregulation of primary cilia function in MHb neurons from HHIP-deficient mice. In addition, many DEGs were targets of POU4F1 (Brn3a), a transcription factor known to be expressed in the brains of adult animals almost exclusively by habenular neurons (57, 68) (*SI Appendix*, Fig. S10). KEGG analysis of cluster-0 DEGs suggested that HHIP deficiency profoundly impacted signaling processes involved in neurotransmission and implicated in nicotine addiction, including cholinergic synapse function (Fig. 3*F*). Likewise, Gene Ontology (GO) analysis of these DEGs suggested that cholinergic transmission was a biological process likely to be dysregulated by HHIP deficiency in MHb neurons (Fig. 3*G*). In contrast to MHb neurons, LHb neurons in cluster 10 contained very few DEGs between *Hhip*$^{+/-}$ and *Hhip*$^{+/+}$ mice (*SI Appendix*, Fig. S9), suggesting that LHb neurons were minimally impacted by HHIP deficiency.

HHIP and PTCH-1 Regulate nAChR Function. The scRNA-seq data from HHIP-deficient animals suggest that HHIP regulates

transcriptional programs involved in cholinergic transmission in MHb neurons. nAChRs are the major class of receptors that regulate cholinergic transmission in the MHb–IPn circuit (15, 69). Thus, we investigated whether HHIP regulates the function of nAChRs, reflected by nAChR-mediated increases in intracellular calcium responses ($[Ca^{2+}]_i$) in human embryonic kidney (HEK) 293 cells preloaded with a calcium-sensitive dye and monitored using a Fluorescent Imaging Plate Reader (FLIPR) instrument. First, we identified a short-hairpin RNA (shRNA-HHIP) that knocked down HHIP expression without inducing toxic effects in HEK 293 cells (*SI Appendix*, Fig. S11). Using shRNA-HHIP, we found that HHIP knockdown markedly decreased $[Ca^{2+}]_i$ evoked by nicotine in HEK 293 cells that stably expressed α4β2α5 nAChRs (Fig. 3 *H* and *I*), considered one of the major nAChR subtypes in the MHb–IPn circuit (19). This was reflected by a decrease in the efficacy (peak response) but not the potency (IC_{50}, concentration that inhibits response by 50%) of nicotine-stimulated $[Ca^{2+}]i$) responses in HHIP-depleted α4β2α5 cells (Fig. 3*I*). Next, we generated a line of HEK 293 cells that stably coexpressed α4β2α5 nAChRs and a Cas9-mCherry fusion protein (α4β2α5::Cas9 cells) (see *Materials and Methods*). Cas9 expression did not impact the health (*SI Appendix*, Fig. S12) or alter the efficacy or potency of nicotine on $[Ca^{2+}]i$ responses in α4β2α5::Cas9 cells compared with parental α4β2α5 cells (Fig. 3*J*). We identified a single-guide RNA (sgRNA) that induced robust genomic cleavage of *HHIP* in α4β2α5::Cas9 cells (sgRNA-HHIP) (*SI Appendix*, Fig. S12) and found that CRISPR/Cas9-mediated *HHIP* cleavage markedly attenuated nicotine-stimulated nAChR signaling (Fig. 3*K*). HHIP functions as a decoy receptor to sequester Hedgehog ligands and thereby promote PTCH-1 activity (34). We found that shRNA-mediated knockdown of PTCH-1 messenger RNA (mRNA) (Fig. 3*L*) or CRISPR/Cas9-mediated genomic cleavage of the *PTCH1* gene (Fig. 3*M*) decreased nAChR signaling similar to HHIP depletion (*SI Appendix*, Fig. S13). How HHIP and PTCH-1 might function together in MHb neurons to regulate nAChR signaling and other neurotransmission-related processes in the absence of core intracellular components of the Hedgehog signaling pathway is unclear. PTCH-1 controls Hedgehog signaling by regulating cholesterol concentration gradients in plasma membrane (28–31), and cholesterol is known to exert a direct inhibitory effect on nAChR signaling (70). Thus, we investigated whether PTCH-1–mediated cholesterol transport influences nAChR signaling. We expressed a PTCH-1 mutant in α4β2α5 cells that contained three amino acid substitutions (D499N, D500N, and E1081Q; NNQ) that prevent conformational changes required for PTCH-1–mediated cholesterol transport without impacting the binding of Hedgehog ligands (PTCH-1-B-NNQ) (31). PTCH-1-B-NNQ expression induced a striking deficit in nAChR signaling in α4β2α5 cells (Fig. 3*N*). A second PTCH-1 mutant containing three amino acid substitutions (I766F, V111F, L114F; IVL) that obstruct the conduit through which cholesterol is transported (PTCH-1-B-IVL) (31) similarly disrupted nAChR signaling in α4β2α5 cells (Fig. 3*N*). Together, these data suggest that HHIP and PTCH-1 regulate nAChR signaling by controlling local cholesterol gradients in the plasma membrane (Fig. 3*O*).

Habenular HHIP Regulates the Motivational Properties of Nicotine. Finally, we investigated whether HHIP acts in the MHb to regulate behavioral responses to nicotine. First, we sought to compare intravenous nicotine self-administration behavior between $Hhip^{+/+}$ and $Hhip^{+/-}$ mice. However, $Hhip^{+/-}$ mice demonstrated profound deficits in their ability to acquire an operant response for food rewards (*SI Appendix*, Fig. S14), consistent with performance-related deficits that render them unsuitable for testing in self-administration procedures. Thus, we instead used the CRISPR/Cas9 system to cleave *Hhip* in the MHb of adult mice. We identified a sgRNA that cleaved the mouse *Hhip* gene with >70% efficiency (sgRNA-Hhip) when cotransfected with Cas9 into mouse N2a cells (Fig. 4 *A*–*C*). GLI-mediated transcription of a luciferase reporter gene was enhanced in N2a cells after sgRNA-Hhip–mediated *Hhip* cleavage (Fig. 4*D*), consistent with abrogated HHIP and PTCH-1 function. We cloned sgRNA-Hhip and a control sgRNA (gRNA-eGFP) into AAV plasmids expressing dTomato and packaged them into infectious particles. We delivered these viruses into the MHb of $Rosa26^{LSL\text{-}spCas9\text{-}eGFP}$ (*STOP-Cas9-eGFP*) mice, in which Cas9 is expressed in a Cre-dependent manner. As HHIP is expressed by both neurons and nonneuronal cells in the MHb (see Fig. 3), we expressed Cas9 selectively in MHb neurons by coinjecting *STOP-Cas9-eGFP* mice with a second AAV that expressed Cre under the control of a neuron-specific promoter (AAV-hSyn1-iCre). Genomic sequencing of habenular tissue confirmed that *Hhip* was efficiently cleaved in the mice treated with AAV-sgRNA-Hhip-dTomato but not AAV-sgRNA-eGFP-dTomato (Fig. 4 *E* and *F*). HHIP protein levels were lower in the MHb of the AAV-sgRNA-Hhip–injected mice compared with AAV-sgRNA-eGFP–injected mice (Fig. 4*F*). In addition, numbers of c-Fos immunoreactive cells were lower in the IPn of AAV-sgRNA-Hhip–injected mice compared with AAV-sgRNA-eGFP–injected mice under baseline conditions (i.e., in the absence of nicotine treatment) (Fig. 4 *G*–*I*). This suggests that CRISPR-mediated HHIP deficiency in the MHb disrupted neural activity in the MHb–IPn circuit, consistent with the dysregulated expression of neurotransmission-related genes we observed in the MHb of HHIP haploinsufficient mice (see Fig. 3). Next, we prepared a new group of *STOP-Cas9-eGFP* mice with intra-MHb injections of AAV-hSyn1-iCre and AAV-sgRNA-eGFP or AAV-sgRNA-Hhip. Six weeks after intra-MHb virus injections, all mice were trained to respond for food rewards (20 mg pellets) under a fixed ratio 5 time-out 20 s (FR5TO20) schedule of reinforcement. No difference in food responding was observed between AAV-sgRNA-Hhip–injected and AAV-sgRNA-eGFP–injected mice (Fig. 4*J*), suggesting that HHIP knockdown in the MHb of adult animals did not precipitate performance-related behavioral deficits similar to those observed in $Hhip^{+/-}$ mice. The AAV-sgRNA-Hhip–injected and AAV-sgRNA-eGFP–injected mice were then permitted to respond for intravenous infusions of nicotine across a broad range of doses (0.03 to 0.8 $mg{\cdot}kg^{-1}$ per infusion) under the same FR5TO20 schedule of reinforcement. Our a priori hypothesis was that manipulating HHIP signaling in the MHb would alter nicotine self-administration behavior in mice only when relatively high unit doses were available for consumption. This hypothesis is based on previously published reports from our laboratory and others showing that MHb neurons regulate nicotine self-administration in rats and mice only when relatively high unit doses of nicotine on the "descending" portion of the dose–response curve are available for consumption (15–20). There was a tendency for AAV-sgRNA-Hhip–treated mice to respond for nicotine infusions at higher rates than AAV-sgRNA-eGFP, which was evidence when relatively high unit doses of nicotine were available for consumption (0.6 to 0.8 $mg{\cdot}kg^{-1}$ per infusion) (Fig. 4*K* and *SI Appendix*, Fig. S15).

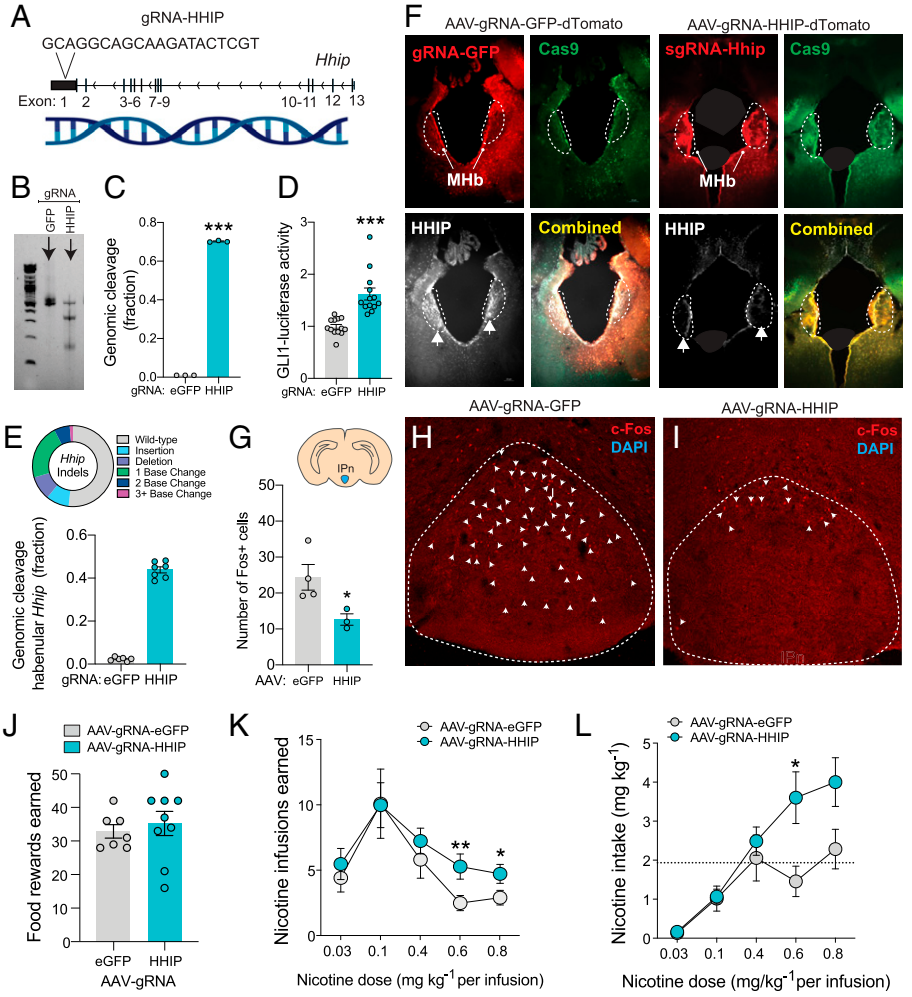

Fig. 4. HHIP in habenula regulates nicotine intake. (*A*) Graphical representation of site in exon 1 of *Hhip* gene targeted by sgRNA-Hhip. (*B*) T7-endonuclease assay using *Hhip* primers showing PCR bands in N2a cells transfected with sgRNA-eGFP or sgRNA-Hhip. (*C*) Fraction of genomic cleavage (mean ± SEM) of *Hhip* in N2a cells after transfection with sgRNA-eGFP-dTomato or sgRNA-Hhip-dTomato; ***$P < 0.001$, unpaired two-sided *t* test. (*D*) sgRNA-Hhip-mediated *Hhip* cleavage increased activity of a GLI1-luciferase reporter in N2a cells; ***$P < 0.001$, unpaired two-sided *t* test. (*E*) Sequenced percentage of genetic indels (mean ± SEM) in *Hhip* gene in MHb of *STOP-spCas9-eGFP* mice >6 wk after stereotaxic injection of AAV-sgRNA-eGFP-dTomato or AAV-sgRNA-Hhip-dTomato in combination with AAV2-hSyn1-iCre.; ***$P < 0.001$, unpaired two-sided *t* test. (*F*) Representative brain slices showing Cas9-eGFP (green), AAV-sgRNA-eGFP/Hhip (red), and HHIP (white) expression in habenula of *ROSA*$^{LSL\text{-}spCas9\text{-}eGFP}$ mice treated with AAV-sgRNA-eGFP-dTomato (*Left*) or AAV-sgRNA-Hhip-dTomato (*Right*). White arrows identify HHIP expression in MHb and highlight reduced relative levels in AAV-sgRNA-Hhip mice. (*G*) Number of c-Fos immunoreactive cells in IPn of *STOP-spCas9-eGFP* mice injected into MHb with AAV2-hSyn1-iCre and AAV-sgRNA-eGFP-dTomato or AAV-sgRNA-Hhip-dTomato >6 wk previously; *$P < 0.05$, unpaired two-sided *t* test. (*H* and *I*) Representative image of c-Fos immunoreactive cells (red; identified by white arrows) in IPn from AAV-sgRNA-eGFP and AAV-sgRNA-Hhip mice. (*J*) Responding for food rewards (mean ± SEM) in by *STOP-spCas9-eGFP* mice injected into MHb with AAV2-hSyn1-iCre and AAV-sgRNA-eGFP-dTomato ($n = 7$) or AAV-sgRNA-Hhip-dTomato ($n = 9$) prior to assessment of their performance in the nicotine self-administration procedure; $P = 0.6058$, unpaired two-sided *t* test. (*K*) Number of nicotine infusions earned (mean ± SEM) by the AAV-sgRNA-eGFP-dTomato and AAV-sgRNA-Hhip-dTomato mice. Main effect of sgRNA: $F_{(1, 14)} = 1.189$, $P = 0.2940$; main effect of nicotine dose: $F_{(4, 56)} = 11.97$, $P = 0.0001$; interaction effect: $F_{(4, 56)} = 0.503$, $P = 0.7336$. (*L*) Total nicotine intake at each unit dose (mean ± SEM) by the AAV-sgRNA-eGFP-dTomato and AAV-sgRNA-Hhip-dTomato mice. Main effect of sgRNA: $F_{(1, 14)} = 3.138$, $P = 0.0983$; main effect of dose: $F_{(4,56)} = 28.59$, $P < 0.0001$; interaction effect: $F_{(4, 56)} = 3.176$, $P = 0.0202$. Bonferroni post hoc comparisons showed that intake was higher in AAV-sgRNA-Hhip-dTomato mice than AAV-sgRNA-eGFP-dTomato mice at the 0.6 mg·kg^{-1} dose of nicotine; *$P = 0.0375$.

When we quantified total amounts of nicotine consumed per session (i.e., number of infusions earned at each unit dose of nicotine multiplied by the dose of nicotine) we found that AAV-sgRNA-Hhip–treated consumed greater amounts of nicotine than AAV-sgRNA-eGFP–treated mice, with this effect evident at the higher unit doses of nicotine on the descending portion of the dose–response curve (Fig. 4*L* and *SI Appendix*, Fig. S15). These data suggest that HHIP acts in the habenula to regulate the motivational properties of nicotine.

Discussion

Major breakthroughs in our understanding of the mechanisms of nicotine addiction have come from genetic studies seeking to identify risk loci for diseases associated with tobacco smoking. For example, large-scale human genetic association studies identified allelic variation in the *CHRNA5–CHRNA3–CHRNB4* gene cluster located in chromosome region 15q25.1, which encodes the α5, α3, and β4 nAChR subunit genes, respectively, as major risk factors for COPD and lung cancer (7, 8, 71–73). These same alleles are also associated with elevated levels of tobacco consumption in individuals who smoke (73–75), likely as a consequence of attenuated stimulatory effects of nicotine on habenular aversion circuits (15–18, 76). Hence, the increased risk of smoking-related lung diseases in those who carry 15q25.1 variant alleles is mediated in part by their relatively high levels of nicotine consumption and greater exposure to disease-causing agents in tobacco smoke (77, 78). Allelic variation in *HHIP* is also associated with smoking-related lung diseases including COPD and lung cancer (6, 10, 37–41). HHIP regulates lung maturation during embryonic development and controls inflammation-related signaling in the lung during adulthood (43, 79). As *HHIP* alleles confer COPD risk even in individuals without a history of smoking (38, 77), it is generally believed that HHIP influences lung diseases independent of tobacco use (80) and its potential involvement in the addiction-related actions of nicotine has not been explored. Here, we report that HHIP is densely expressed by MHb neurons, particularly MHb cholinergic neurons, which are known to regulate nicotine aversion (15–17, 19–21, 76). We found that HHIP deficiency dysregulated the expression of genes involved in cholinergic transmission and other neurotransmission-related processes in MHb neurons. We also found that HHIP regulates nAChR signaling by a mechanism likely involving PTCH-1–mediated control of cholesterol concentration gradients in the plasma membrane. Finally, we observed that CRISPR-mediated knockdown of HHIP in MHb neurons increased nicotine self-administration behavior in mice. These findings suggest that, in addition to its important role in the maintenance and repair of

lung tissue, HHIP may influence the risk of smoking-related lung diseases by controlling the actions of nicotine on habenular aversion circuits.

HHIP expressed on cell surfaces or secreted into the extracellular milieu sequesters Hedgehog ligands to facilitate PTCH-1 activity and thereby suppress SMO/GLI-mediated Hedgehog signaling. We found that HHIP and PTCH-1 are densely expressed by MHb neurons in adult mice, where it would be expected to control Hedgehog signaling. However, MHb neurons expressed SMO and GLI transcription factors at very low or undetectable levels, and we were unable to detect GLI-mediated transcriptional activity in the MHb–IPn circuit of mice or rats. Hedgehog signaling is known to regulate the formation of the MHb during embryonic development by coordinating the activity of GLI, POU4F1, TCF7L2, and other related transcription factors (68, 81–83). Thus, Hedgehog signaling appears to undergo a developmental switch in which canonical SMO/GLI-mediated transcription becomes quiescent during the postnatal period (19), even though mature MHb neurons continue to express receptors for Hedgehog ligands. We did not observe any overt structural abnormalities in the MHb–IPn circuit of HHIP haploinsufficient mice, although we harvested much higher numbers of astrocytes and microglia from the habenula of the haploinsufficient mice compared with wild-type mice. Genes involved in cholinergic transmission and other neurotransmission-related processes were dysregulated in MHb neurons from the haploinsufficient animals. This suggests that HHIP and PTCH-1 expressed on the surface of adult MHb neurons is not a vestigial artifact devoid of functional consequence. Instead, HHIP and PTCH-1 likely signal through SMO/GLI-independent noncanonical mechanisms to regulate transcriptional programs in adult MHb neurons. Consistent with this possibility, we found that HHIP and PTCH-1 regulate nAChR signaling by a mechanism involving fluctuations in cholesterol gradients in the plasma membrane of nAChR-expressing cells. MHb neurons express some of the highest concentrations of nAChRs in the mammalian brain, and cholesterol directly interacts with nAChRs to modulate their function (70, 84). Thus, HHIP and PTCH-1 may be expressed at such high levels by MHb neurons, particularly MHb^{Chat} neurons, to titrate nAChR signaling through cholesterol-dependent processes in response to Shh and other Hedgehog ligands secreted by septal afferents. Besides nAChRs, membrane cholesterol gradients regulate the function of many other neurotransmitter receptors and play important roles in organizing signal transduction domains on the surface of neurons (85). Hence, the dysregulated transcriptomes in MHb neurons from HHIP haploinsufficient mice likely reflect perturbation of cholesterol-controlled signaling processes, which modifies the activity of POU4F1 and other non-GLI transcription factors. Notably, PTCH-1 localizes to primary cilia in neurons and other cells to regulate downstream signaling pathways (86), and many of the dysregulated genes in MHb neurons from nicotine-treated or HHIP-deficient mice were predicted to be regulated by cilia-associated signaling pathways. Cilia on MHb cells are thought to detect regulatory factors (growth factors, hormones, etc.) and xenobiotic agents contained in the cerebrospinal fluid (CSF) of the third ventricle (59, 87). Thus, it is an interesting possibility that HHIP/PTCH-1 signaling in primary cilia regulates the detection by MHb neurons of nicotine contained in CSF and to engage nicotine avoidance behaviors.

In summary, our data demonstrate that HHIP is expressed by MHb cholinergic neurons, which play an important role in nicotine aversion (19–21), and that knockdown of HHIP expression in the MHb enhances the motivational properties of nicotine. These findings suggest that HHIP may influence the risk of developing smoking-related lung diseases in part by regulating the stimulatory effects of nicotine on habenula aversion circuits.

Materials and Methods

Animals. Male and female C57BL6J mice (JAX Stock #: 000664), $ROSA^{LSL\text{-}spCas9\text{-}eGFP}$ mice (JAX Stock no. 026175), $Chat^{DW167}$ TRAP mice (JAX Stock no. 030250), $HHIP^{tm1Amc}$/J ($HHIP^{+/-}$) mice (JAX Stock no. 006241) were obtained from Jackson Laboratories and bred in our animal facility according to Jackson breeding instructions. For fiber photometry, *Gpr151-Cre* mice containing random insertion of bacterial artificial chromosome (BAC) clone MSMg01-81G4 was kindly provided by S. Itohara (RIKEN Brain Science Institute Saitama, Japan) and maintained on a C57BL6/J background (JAX Stock no. 000664). Mice were housed two to five per cage and were >8 wk of age at time of experiments. Male Wistar rats were purchased from Charles River and housed in pairs. Male and female mice were included in experiments to ensure that sex as an independent biological variable was represented. Sex-related differences in experimental endpoint were not apparent. All rodents were maintained in an American Association for Laboratory Animal Care–accredited vivarium on a 12-h reverse light-dark cycle. All animal procedures were approved by the Institutional Animal Care and Use Committee of the Icahn School of Medicine at Mount Sinai.

Drugs. Nicotine bitartrate dihydrate (MP Biomedicals LLC, catalog no. 0521149910) was dissolved in saline and the pH adjusted to 7.6 with NaOH. Nicotine solutions were prepared daily in glass vials wrapped in aluminum foil to protect from light and sterilized by being passed through a 0.25-μm syringe filter (Fisher Scientific, catalog no. 09-719C). Nicotine doses are reported as free base. Recombinant HHIP protein was purchased from R&D systems (catalog no. 1568-HP). Murine Shh protein (catalog no. 315-22) and human Shh protein (catalog no. 100-45) were purchased from Preprotech and used at a final concentration of 3 $\mu g \cdot mL^{-1}$.

Plasmids and Viruses. Plasmid and packaged lentivirus particles containing the pGreenFire1-Gli (EF1α-neo) Lentivector reporter were purchased from System Biosciences (catalog nos. TR050pa-N and TR050VA-N, respectively). pcDNA-h-mmPtch1-B-V111FL114FI766F-HA-TagBFP and pcDNA-h-mmPtch1-B-NNQ-HA-GFP were gifts from Philip Beachy (Stanford University School of Medicine, Stanford, CA 94305; Addgene plasmids 121164 and 120911, respectively). sgRNAs for in vivo CRISPR experiments were cloned into a modified version of Addgene plasmid 60229 donated by the Zhang laboratory: AAV:ITR-U6-sgRNA(backbone)-pCBh-Cre-WPRE-hGHpA-ITR in which the Cre recombinase cassette was removed. The sgRNA of interest (HHIP or eGFP) was cloned in to an AAV1 serotype by Vector Biolabs. The HHIP sgRNA sequence on the antisense strand was GCAGGCAGCAAGATACTCGT. The control AAV contained an sgRNA targeting a sequence in the eGFP gene previously assessed by the Zhang laboratory. The sequence of the eGFP sgRNA was GAGCTGGACGGCGACGTAAA (88). Details about these viruses are provided in the following table:

AAV	Company	Catalog no.	Serotype	Titer*
AAV-sgRNA-Hhip	Vector Biolabs packaged from modified Addgene plasmid 60229	Addgene plasmid 60229	AAV1	3.5×10^{13} GC/mL
AAV-sgRNA-eGFP	Vector Biolabs packaged from modified Addgene plasmid 60229	Addgene plasmid 60229	AAV1	3.6×10^{13} GC/mL
AAV-hSyn1-iCre	Vector Biolabs	VB1088	AAV2	1.7×10^{13} GC/mL
AAV-Flex-GCaMP6m	Addgene	100838-AAV1	AAV1	1.1×10^{13} GC/mL
Lenti-pGreen Fire1-Gli (EF1αneo)	System Biosciences	TR050VA-N	Lenti	$>2 \times 10^{9}$ IFUs

*GC, genome copies; IFUs, infectious units.

Stereotaxic Surgeries and Intracranial Injections. We used the following stereotaxic coordinates to target the MHb in *Gpr151*-Cre mice for fiber photometry experiments: anterior–posterior (AP): −1.33; medial–lateral (ML): 0.60; dorsal–ventral (DV): −2.5; 5° angle from midline. The injector needle remained in place for 2 min after injection of AAV-GCaMP6m (200 nL per side). Immediately afterward, optical fibers were implanted into MHb: AP: −1.3; ML: 0.55; DV: −2.25; 5° angle from midline. AAVs were injected into the MHb of $ROSA^{LSL\text{-}spCas9\text{-}eGFP}$ mice for HHIP knockdown according to the following stereotaxic coordinates: AP: −1.55; ML: ±1.65; DV from dura: −2.9 (100 nL/AAV) and −3.0 (100 nL/AAV); angle: 32° from midline. Wistar rats were implanted with a guide cannula (Plastics One) positioned 2 mm above the IPn (10° angle toward the midline, AP: 6.72 mm from bregma; ML: 1.6 mm from midline; DV: 6.5 mm from brain surface). The IPn was infused with recombinant HHIP protein (R&D Systems, catalog no. 1568-HP) (100 ng dissolved in 0.1 M phosphate-buffered saline [PBS] infused over 1 min, 10 min prior to the session). These same coordinates were used to deliver a lentivirus (>2 × 10^6 infectious units [IFUs]; 600 nL) in the IPn of rats to express the pGreenFire1-Gli (EF1α-neo) Lentivector reporter (System Biosciences, catalog no. TR050VA-N).

Fiber Photometry. An AAV expressing GCaMP6m in a Cre-dependent manner was infused into the MHb of *Gpr151*-Cre mice ($n = 6$ males, 12 to 16 wk). To facilitate adaptation to photometry recordings, mice were trained with the fiber optic cable connected without recording for two or three sessions (∼30 min). Photometry recordings commenced >3 wk after virus injection and optical fiber implantation. Mice were allowed to freely explore their home cage during recording. The recording included 3 min of baseline recording, followed by saline injection with a subsequent recording of ∼2 min, after which time nicotine was injected. Fluorescence signals were collected using a DORIC system at a sampling frequency of 12 kilosamples per second. Light-emitting diode (LED) power was maintained at the same level across recording sessions and animals. The fluorescence signal in each animal was normalized by calculating ΔF/F values (F465 − F405)/F405) using a custom-made MATLAB analysis pipeline (available at https://github.com/SCaligiuri/Photometry-Analysis-by-VM-CF). The deviation of each sample from the averaged signal was calculated with a Z-score.

scRNA-Seq and Differential Gene Expression Analyses. Male and female C57BL6J mice ($n = 12$ in total) aged 12 to 15 wk of age were injected with saline ($n = 6$ in total; half male and half female) or nicotine (1.0 $mg{\cdot}kg^{-1}$ SC; $n = 6$ in total; half male and half female) for three consecutive days. Mice were killed 24 h after the final injection by cervical dislocation, their brains rapidly removed, and habenulae dissected on ice using a 1-mm tissue punch (Integra Miltex catalog no. 33-31AA-P/25). Hhiptm1Amc/J mice (Jackson Laboratories, stock no. 006241) were bred by heterozygous mating with wild-type (C57BL6J) mice. $Hhip^{+/+}$ ($n = 3$ male and $n = 3$ female) and $Hhip^{+/-}$ ($n = 3$ male and $n = 3$ female) mice aged 12 to 15 wk were injected with saline for three consecutive days to control for injection-related stress and permit comparison with data from the saline- and nicotine-treated mice described above. Mice were killed 24 h after the last injection via cervical dislocation and habenulae collected as described above. Habenular tissue was immediately processed for scRNA-seq according to the protocol from 10x Genomics. Single cells were isolated using enzymatic and mechanical disaggregation and scRNA-seq was performed using the Chromium platform from 10x Genomics. Libraries were sequenced in paired end mode on a NovaSeq instrument (Illumina) to a targeting a depth of 50,000 to 100,000 reads per cell. Sequencing data were aligned and quantified using the Cell Ranger Single-Cell Software Suite (version 3.1, 10x Genomics) against the mm10 mouse reference genome. Samples were merged using Cell Ranger and sequencing read depth normalized across samples. Clustering and gene expression analyses was performed using ScanPy (v1.5.1) and custom Python code (https://github.com/alexcwsmith/singleCellTools). A more detailed description scRNA-seq methods and analysis is provided in *SI Appendix*.

TRAP-Seq. MHb tissue from $Chat^{DW167}$ mice was pooled (three or four mice for each sample; male and female 14 to 18 wk old), and TRAP was performed in triplicate. Libraries were prepared using the Ovation V2 RNA-seq Kit from NuGen and sequenced on the Illumina HiSEq. 2500. RNA-seq reads were aligned to the UCSC mm10 reference genome using STAR (89), version 2.3.0e_r291, with default settings. Quantification of aligned reads was performed using htseq-count module, part of the HTSeq framework (90), version 0.6.0, with "union" mode to handle reads overlapping more than one feature. Gene lists were then further filtered for BaseMean reads >100 to exclude genes with low expression.

RNAscope Fluorescent In Situ Hybridization. Male C57BL/6J mice aged 8 wk or older were anesthetized with isoflurane and decapitated and their brains collected and immediately frozen in isopentane over dry ice. Coronal brain sections (14 to 16 μm) were prepared using a cryostat (Leica Biosystems) at −18 to −21 °C. Fluorescent in situ hybridization was performed using the RNAscope Multiplex Detection V1 kit with probes for *Hhip*, *Chat*, *Olig2*, and *Slc17a6* transcripts (448441, 408731-C2, 447091-C3, and 319171-C3, respectively) from Advanced Cell Diagnostics following manufacturer's instructions with the following probe/fluorophore pairs: *Hhip*, Atto550 (Cy3); *Chat*, Alexa488 (eGFP); *Olig2*, Atto 647 (Cy5); *Slc17a6*, Atto 647 (Cy5). Further methodological details are reported in *SI Appendix*.

Real-Time PCR. Samples were reverse-transcribed into complementary DNA using the TaqMan High-Capacity cDNA Reverse Transcription kit (Thermo Fisher Scientific, catalog no. 4374966). Complementary DNA (cDNA) was combined with TaqMan MasterMix (Thermo Fisher Scientific, catalog no. 4369016) to perform mouse *Hhip* (Mm00469580_m1 Hhip) or *ActB* (Mm02619580_g1) gene expression assays (Thermo Fisher Scientific) using RT-PCR (QuantStudio 7 Flex, Applied Biosystems, Life Technologies). *Hhip* expression was normalized to *ActB* and comparison between groups was made using the method of $2^{-\Delta\Delta Ct}$.

Murine *Hhip* TaqMan probe sequence spanning exons 12 to 13 was GTGTGAGCCAGCGTGCCGTCATGGAGGTGTCTGTGTCAGACCGAACAAGTGCCTCTGTAAAAAGGGCTAT.

Murine *ActB* TaqMan probe sequence spanning exon 3 was CACACCTTCTACAATGAGCTGCGTGTGGCCCCTGAGGAGCACCCTGTGCTGCTCACCGAGGCCCCCCTGAACCCTAAGGCCAACCGTGAAAAGATGACCCAGATCATGTTTGAGACCTTCAACACCCCAGCCATGTACGTAGC.

Immunohistochemistry. Animals for immunohistochemistry were anesthetized with an isoflurane (1 to 3%)/oxygen vapor mixture and perfused through the ascending aorta with cold 0.1 M PBS, followed by 4% paraformaldehyde (PFA) in 0.1 M PBS (pH 7.4). Brains were collected, postfixed overnight in 4% PFA in 0.1 M PBS, and then cryoprotected in 30% sucrose in 0.1 M PBS (pH 7.4) for 72 h at 4 °C. The cryoprotected brains were embedded in Tissue-Tek OCT compound (Finetek). Thirty-micrometer coronal sections were cut on a cryostat and collected directly onto superfrost plus slides (ThermoFisher, catalog no. 22037246). Following antibody staining for HHIP, PTCH-1, or c-Fos, immunoreactive cells were visualized with a Zeiss AxioImager Z3 epifluorescence microscope using 5× or 20× Plan-APOCHROMAT (Zeiss, 420650-9901) objective lenses combined with LED illumination (Lumencor Light Engine, SOLA SM 5-LCR-SA). Reflectors for blue fluorescent protein, red fluorescent protein, green fluorescent protein, and infrared Cy5 were used. Images were captured by a digital charge-coupled device camera (Orca-R2, Hamamatsu, C10600) using 1 × 1 binning and consistent exposure times for all channels. Immunoreactive positive cells were observed in a treatment-blinded manner. Details about antibody staining procedures are available in *SI Appendix, Supplemental Methods*.

GLI1-Reporter Assays in Brain Slices. N2a-Gli reporter cells (details on cells available in *SI Appendix, Supplemental Methods*) were plated at 0.05 × 10^6 cells/well in 24-well plates and transfected with Control or *Hhip*-targeting sgRNAs (same sgRNA sequence for in vivo: GCAGGCAGCAAGATACTCGT) and spCas9 mRNA (Thermo Fisher catalog no. A29378) using Lipofectamine Messenger max (Thermo Fisher Scientific, catalog no. LMRNA001). Seventy-two hours posttransfection, cells were assessed for luciferase activity using the Britelite assay system as per the manufacturer's instruction (PerkinElmer, catalog no. 6066761). Luminescence was measured with the Cytation 3 BioTek Imaging Reader; cells transfected with control scramble were compared to knockdown. Adult male Wistar rats ($n = 6$) were injected into the IPn with a lentivirus (>2 × 10^6 IFUs; 600 nL) to express the pGreenFire1-Gli (EF1α-neo) Lentivector reporter (System Biosciences, catalog no. TR050VA-N). More than 3 wk later, rats were injected with luciferin (150 $mg{\cdot}kg^{-1}$ intraperitoneally) dissolved in sterile 0.9% saline (25 $mg{\cdot}mL^{-1}$). Twenty minutes later, rats were anesthetized with an isoflurane/oxygen vapor mixture and brains rapidly dissected on ice. Coronal slices

(about 1.5 mm; one or two in total) were collected from each animal to include the full extent of the IPn. All imaging was performed using the IVIS Spectrum imaging module from Caliper Life Sciences. Imaging experiments began following an addition of luciferin (at a concentration of 0.3 mg·mL^{-1}) to characterize "baseline" luminance. To stimulate GLI activity, recombinant Shh protein (final concentration 3 μg/mL) was added to the bath and reads were collected every 5 min over the next 30 min. A total of seven regions of interest (ROIs) from six rats was used for statistical analyses. Further details are available in *SI Appendix, Supplemental Methods*.

Tissue Culture and Cell Lines. HEK 293 cells stably expressing α4β2α5 nAChRs were a generous gift from Jon Lindstrom (University of Pennsylvania). HEK cells were cultured in Dulbecco's modified Eagle's medium (DMEM) containing 25 mM Hepes, 2 mM glutamine, 1 mM pyruvate, 10% fetal bovine serum (FBS) (Gibco), and 1% penicillin/streptomycin (pen/strep). Mouse neuroblastoma N2a cells were purchased from ATCC (CCL-131, American Type Culture Collection) and cultured in DMEM media supplemented with 10% FBS, 1% pen/strep.

Cell-Based Functional Assays. Details about cell-based fluorescent intracellular calcium assay and GLI1-luciferase reporter assay are available in *SI Appendix, Supplemental Methods*.

shRNA-Mediated Knockdown of HHIP and PTCH-1. HEK cells stably expressing α4β2α5 nAChRs (91) were used to assess HHIP knockdown after transfection with shRNA-expressing plasmids (pLKO.1-puro: 10 μg of Scrambled/shRNA) was used in 100-mm dishes and cells were assessed for knockdown and/or calcium 48 and 72 h posttransfection. ShRNAs directed against human *HHIP* transcripts from the Mission shRNA library (Sigma-Aldrich) were used (clones E8, E9, E10, E11, and E12). PTCH-1 expression was similarly assessed in α4β2α5 nAChR HEKs after transfection with shRNAs against human *PTCH1* transcripts from the Mission shRNA library (clones C2, C3, C4, C5, and C6). Expression was assessed 48 h after transfection via TaqMan PCR using the $2^{-\Delta\Delta Ct}$ method and GAPDH expression for normalization. Additional details are available in *SI Appendix, Supplemental Methods*.

Genomic Cleavage of HHIP and PTCH-1 in HEK Cells. HEK 293 cells stably expressing α4β2α5 nAChRs (91) were transfected with the FUCas9mCherry plasmid from Addgene (catalog no. 70182) and a clonal line (α4β2α5::Cas9 HEKs) was identified and validated for CRISPR/Cas9 experiments. We identified sgRNAs that efficiently cleaved the human *HHIP* or *PTCH1* gene in in these cells, as measured using the T7 endonuclease-based assay (Thermo Fisher, catalog no. A24373). Details about the generation of α4β2α5::Cas9 cells and validation of sgRNAs are available in *SI Appendix, Supplemental Methods*.

Genomic Cleavage of HHIP in Mouse Brain. To target the mouse *Hhip* gene, three sgRNAs were designed (crispor.tefor.net/), synthesized (Thermo Fisher sgRNA synthesis kit, catalog no. A29377), and tested for genomic cleavage efficiency in mouse N2a cells using the T7 endonuclease-based assay (Thermo Fisher, catalog no. A24373). An sgRNA directed against the anti-sense strand of *Hhip* (GCAGGCAGCAAGATACTCGT) efficiently cleaved *Hhip* and increased GLI1-luciferase reporter activity in mouse N2a cells. This sgRNA was packaged into AAV particles for in vivo experiments. AAV details are included in *Stereotaxic Surgeries and Intracranial Injections*. Further details are available in *SI Appendix, Supplemental Methods*.

Intravenous Nicotine Self-Administration. *ROSA*$^{LSL\text{-}spCas9\text{-}eGFP}$ mice aged 8 to 12 wk were injected into the MHb with AAV-hSyn-iCre and AAV-sgRNA-Hhip or AAV-sgRNA-eGFP. Male Wister rats ($n = 20$) were prepared with a chronic indwelling cannula located above the IPn for intracranial injections >6 wk after AAV injections in mice and >1 wk after cannula implantation in rats; mice and rats were trained to respond for food rewards under a fixed-ratio 5, time-out 20 s (FR5TO20) schedule of reinforcement during 60-min daily sessions, prepared with intravenous jugular catheters, then permitted to respond under the same FR5TO20 schedule for nicotine infusions. Details about surgical, training, and testing procedures are provided in *SI Appendix, Supplemental Methods*.

Statistical Analyses. Gaussian distribution of data was tested using the Shapiro–Wilk test in GraphPad Prism. Normally distributed data were analyzed by one- or two-way ANOVA or two-tailed *t* test as appropriate, using GraphPad Prism or Statistical Analysis Software (SAS version 9.4). Significant main or interaction effects were followed by multiple comparison post hoc tests (Bonferroni, Newman–Keuls, or Tukey) as recommended by GraphPad Prism. Direct pairwise comparisons of responding for nicotine infusions between groups of mice in the self-administration experiment were also made by unpaired two-tailed *t* test. Nonnormally distributed data were analyzed by Mann–Whitney *U* test, as indicated in figure legends. Fisher's exact test was used to compare categorical data such as cell clustering in scRNA-seq analyses. KEGG, GO, and GWAS Catalog analyses of DEGs identified by scRNA-seq were performed using Enrichr (https://maayanlab.cloud/Enrichr/). Upstream regulator analysis of DEGs was performed using Ingenuity Pathway Analysis. The nonlinear regression curve-fitting feature in GraphPad Prism was used to generate dose–response curves for intracellular calcium data generated using FLIPR (best-fit values). Peak response and IC_{50} values were compared between treatment groups using extra sum-of-squares *F* tests. All data are expressed as mean ± SEM.

Data, Materials, and Software Availability. Single-cell RNA sequencing data have been deposited in Gene Expression Omnibus, GSE217000 (92). All other study data are included in the article and/or *SI Appendix*.

ACKNOWLEDGMENTS. This work was supported by grants from the National Institute on Drug Abuse (DA020686, DA045649, and DA053629 to P.J.K.) and by the Canadian Institutes of Health Research Post-Doctoral Fellowship (to S.P.B.C).

1. G. B. D. T. Collaborators; GBD 2015 Tobacco Collaborators, Smoking prevalence and attributable disease burden in 195 countries and territories, 1990-2015: A systematic analysis from the Global Burden of Disease Study 2015. *Lancet* **389**, 1885–1906 (2017).
2. B. Lamprecht *et al.*; BOLD Collaborative Research Group, COPD in never smokers: Results from the population-based burden of obstructive lung disease study. *Chest* **139**, 752–763 (2011).
3. I. P. Stolerman, M. J. Jarvis, The scientific case that nicotine is addictive. *Psychopharmacology (Berl.)* **117**, 2–10, discussion 14–20 (1995).
4. C. D. Fowler, P. J. Kenny, Nicotine aversion: Neurobiological mechanisms and relevance to tobacco dependence vulnerability. *Neuropharmacology* **76**, 533–544 (2014).
5. M. A. Russell, C. Wilson, U. A. Patel, C. Feyerabend, P. V. Cole, Plasma nicotine levels after smoking cigarettes with high, medium, and low nicotine yields. *BMJ* **2**, 414–416 (1975).
6. S. G. Pillai *et al.*; ICGN Investigators, A genome-wide association study in chronic obstructive pulmonary disease (COPD): Identification of two major susceptibility loci. *PLoS Genet.* **5**, e1000421 (2009).
7. R. J. Hung *et al.*, A susceptibility locus for lung cancer maps to nicotinic acetylcholine receptor subunit genes on 15q25. *Nature* **452**, 633–637 (2008).
8. C. I. Amos *et al.*, Genome-wide association scan of tag SNPs identifies a susceptibility locus for lung cancer at 15q25.1. *Nat. Genet.* **40**, 616–622 (2008).
9. M. H. Cho *et al.*; NETT Genetics, ICGN, ECLIPSE and COPDGene Investigators, Risk loci for chronic obstructive pulmonary disease: A genome-wide association study and meta-analysis. *Lancet Respir. Med.* **2**, 214–225 (2014).
10. I. A. Yang, J. W. Holloway, K. M. Fong, Genetic susceptibility to lung cancer and co-morbidities. *J. Thorac. Dis.* **5** (suppl. 5), S454–S462 (2013).
11. C. Mulle, D. Choquet, H. Korn, J. P. Changeux, Calcium influx through nicotinic receptor in rat central neurons: Its relevance to cellular regulation. *Neuron* **8**, 135–143 (1992).
12. L. Lecourtier, P. H. Kelly, A conductor hidden in the orchestra? Role of the habenular complex in monoamine transmission and cognition. *Neurosci. Biobehav. Rev.* **31**, 658–672 (2007).
13. O. Hikosaka, The habenula: From stress evasion to value-based decision-making. *Nat. Rev. Neurosci.* **11**, 503–513 (2010).
14. C. G. Baddick, M. J. Marks, An autoradiographic survey of mouse brain nicotinic acetylcholine receptors defined by null mutants. *Biochem. Pharmacol.* **82**, 828–841 (2011).
15. C. D. Fowler, Q. Lu, P. M. Johnson, M. J. Marks, P. J. Kenny, Habenular α5 nicotinic receptor subunit signalling controls nicotine intake. *Nature* **471**, 597–601 (2011).
16. S. Frahm *et al.*, Aversion to nicotine is regulated by the balanced activity of β4 and α5 nicotinic receptor subunits in the medial habenula. *Neuron* **70**, 522–535 (2011).
17. B. Forget *et al.*, A human polymorphism in CHRNA5 is linked to relapse to nicotine seeking in transgenic rats. *Curr. Biol.* **28**, 3244–3253.e7 (2018).
18. K. S. Elayouby *et al.*, α3* nicotinic acetylcholine receptors in the habenula-interpeduncular nucleus circuit regulate nicotine intake. *J. Neurosci.* **41**, 1779–1787 (2021).
19. A. Duncan *et al.*, Habenular TCF7L2 links nicotine addiction to diabetes. *Nature* **574**, 372–377 (2019).
20. L. M. Tuesta *et al.*, GLP-1 acts on habenular avoidance circuits to control nicotine intake. *Nat. Neurosci.* **20**, 708–716 (2017).
21. S. Frahm *et al.*, An essential role of acetylcholine-glutamate synergy at habenular synapses in nicotine dependence. *eLife* **4**, e11396 (2015).
22. B. R. Myers, L. Neahring, Y. Zhang, K. J. Roberts, P. A. Beachy, Rapid, direct activity assays for Smoothened reveal Hedgehog pathway regulation by membrane cholesterol and extracellular sodium. *Proc. Natl. Acad. Sci. U.S.A.* **114**, E11141–E11150 (2017).
23. R. Petrova, A. L. Joyner, Roles for Hedgehog signaling in adult organ homeostasis and repair. *Development* **141**, 3445–3457 (2014).

24. V. Marigo, R. A. Davey, Y. Zuo, J. M. Cunningham, C. J. Tabin, Biochemical evidence that patched is the Hedgehog receptor. *Nature* **384**, 176–179 (1996).
25. R. L. Johnson *et al.*, Human homolog of patched, a candidate gene for the basal cell nevus syndrome. *Science* **272**, 1668–1671 (1996).
26. M. van den Heuvel, P. W. Ingham, Smoothened encodes a receptor-like serpentine protein required for hedgehog signalling. *Nature* **382**, 547–551 (1996).
27. J. Alcedo, M. Ayzenzon, T. Von Ohlen, M. Noll, J. E. Hooper, The Drosophila smoothened gene encodes a seven-pass membrane protein, a putative receptor for the hedgehog signal. *Cell* **86**, 221–232 (1996).
28. J. Taipale, M. K. Cooper, T. Maiti, P. A. Beachy, Patched acts catalytically to suppress the activity of Smoothened. *Nature* **418**, 892–897 (2002).
29. M. Bidet *et al.*, The hedgehog receptor patched is involved in cholesterol transport. *PLoS One* **6**, e23834 (2011).
30. P. Huang *et al.*, Cellular cholesterol directly activates smoothened in hedgehog signaling. *Cell* **166**, 1176–1187.e14 (2016).
31. Y. Zhang *et al.*, Structural basis for cholesterol transport-like activity of the hedgehog receptor patched. *Cell* **175**, 1352–1364.e14 (2018).
32. N. Denef, D. Neubüser, L. Perez, S. M. Cohen, Hedgehog induces opposite changes in turnover and subcellular localization of patched and smoothened. *Cell* **102**, 521–531 (2000).
33. A. Ruiz i Altaba, Gli proteins and Hedgehog signaling: Development and cancer. *Trends Genet.* **15**, 418–425 (1999).
34. P. T. Chuang, A. P. McMahon, Vertebrate Hedgehog signalling modulated by induction of a Hedgehog-binding protein. *Nature* **397**, 617–621 (1999).
35. S. C. Griffiths *et al.*, Hedgehog-Interacting Protein is a multimodal antagonist of Hedgehog signalling. *Nat. Commun.* **12**, 7171 (2021).
36. A. M. Holtz *et al.*, Secreted HHIP1 interacts with heparan sulfate and regulates Hedgehog ligand localization and function. *J. Cell Biol.* **209**, 739–757 (2015).
37. X. Zhou *et al.*, Identification of a chronic obstructive pulmonary disease genetic determinant that regulates HHIP. *Hum. Mol. Genet.* **21**, 1325–1335 (2012).
38. E. Repapi *et al.*; Wellcome Trust Case Control Consortium; NSHD Respiratory Study Team, Genome-wide association study identifies five loci associated with lung function. *Nat. Genet.* **42**, 36–44 (2010).
39. D. B. Hancock *et al.*, Meta-analyses of genome-wide association studies identify multiple loci associated with pulmonary function. *Nat. Genet.* **42**, 45–52 (2010).
40. Y. M. Van Durme *et al.*, Hedgehog-interacting protein is a COPD susceptibility gene: The Rotterdam Study. *Eur. Respir. J.* **36**, 89–95 (2010).
41. R. P. Young *et al.*, Chromosome 4q31 locus in COPD is also associated with lung cancer. *Eur. Respir. J.* **36**, 1375–1382 (2010).
42. P. T. Chuang, T. Kawcak, A. P. McMahon, Feedback control of mammalian Hedgehog signaling by the Hedgehog-binding protein, Hip1, modulates Fgf signaling during branching morphogenesis of the lung. *Genes Dev.* **17**, 342–347 (2003).
43. T. Lao *et al.*, Hhip haploinsufficiency sensitizes mice to age-related emphysema. *Proc. Natl. Acad. Sci. U.S.A.* **113**, E4681–E4687 (2016).
44. D. A. van der Plaat *et al.*, Genome-wide association study on the FEV_1/FVC ratio in never-smokers identifies HHIP and FAM13A. *J. Allergy Clin. Immunol.* **139**, 533–540 (2017).
45. S. M. Lutz *et al.*; ECLIPSE Investigators; COPDGene Investigators, A genome-wide association study identifies risk loci for spirometric measures among smokers of European and African ancestry. *BMC Genet.* **16**, 138 (2015).
46. M. Soler Artigas *et al.*; International Lung Cancer Consortium; GIANT consortium, Genome-wide association and large-scale follow up identifies 16 new loci influencing lung function. *Nat. Genet.* **43**, 1082–1090 (2011).
47. D. A. McCormick, D. A. Prince, Acetylcholine causes rapid nicotinic excitation in the medial habenular nucleus of guinea pig, in vitro. *J. Neurosci.* **7**, 742–752 (1987).
48. P. Y. Shih *et al.*, Differential expression and function of nicotinic acetylcholine receptors in subdivisions of medial habenula. *J. Neurosci.* **34**, 9789–9802 (2014).
49. R. A. Lester, J. A. Dani, Time-dependent changes in central nicotinic acetylcholine channel kinetics in excised patches. *Neuropharmacology* **33**, 27–34 (1994).
50. L. Wills *et al.*, Neurobiological mechanisms of nicotine reward and aversion. *Pharmacol. Rev.* **74**, 271–310 (2022).
51. Y. Kobayashi *et al.*, Genetic dissection of medial habenula-interpeduncular nucleus pathway function in mice. *Front. Behav. Neurosci.* **7**, 17 (2013).
52. B. Antolin-Fontes *et al.*, The habenular G-protein-coupled receptor 151 regulates synaptic plasticity and nicotine intake. *Proc. Natl. Acad. Sci. U.S.A.* **117**, 5502–5509 (2020).
53. F. A. Wolf, P. Angerer, F. J. Theis, SCANPY: Large-scale single-cell gene expression data analysis. *Genome Biol.* **19**, 15 (2018).
54. J. Carlson, K. Noguchi, G. Ellison, Nicotine produces selective degeneration in the medial habenula and fasciculus retroflexus. *Brain Res.* **906**, 127–134 (2001).
55. J. Carlson, B. Armstrong, R. C. Switzer, 3rd, G. Ellison, Selective neurotoxic effects of nicotine on axons in fasciculus retroflexus further support evidence that this a weak link in brain across multiple drugs of abuse. *Neuropharmacology* **39**, 2792–2798 (2000).
56. M. L. Wallace *et al.*, Anatomical and single-cell transcriptional profiling of the murine habenular complex. *eLife* **9**, e51271 (2020).
57. Y. Hashikawa *et al.*, Transcriptional and spatial resolution of cell types in the mammalian habenula. *Neuron* **106**, 743–758.e5 (2020).
58. Z. Anvarian, K. Mykytyn, S. Mukhopadhyay, L. B. Pedersen, S. T. Christensen, Cellular signalling by primary cilia in development, organ function and disease. *Nat. Rev. Nephrol.* **15**, 199–219 (2019).
59. B. Le Foll, L. French, Transcriptomic characterization of the human habenula highlights drug metabolism and the neuroimmune system. *Front. Neurosci.* **12**, 742 (2018).
60. J. L. Ables *et al.*, Retrograde inhibition by a specific subset of interpeduncular α5 nicotinic neurons regulates nicotine preference. *Proc. Natl. Acad. Sci. U.S.A.* **114**, 13012–13017 (2017).
61. A. Görlich *et al.*, Reexposure to nicotine during withdrawal increases the pacemaking activity of cholinergic habenular neurons. *Proc. Natl. Acad. Sci. U.S.A.* **110**, 17077–17082 (2013).
62. R. Salas, R. Sturm, J. Boulter, M. De Biasi, Nicotinic receptors in the habenulo-interpeduncular system are necessary for nicotine withdrawal in mice. *J. Neurosci.* **29**, 3014–3018 (2009).
63. J. D. Dougherty, E. F. Schmidt, M. Nakajima, N. Heintz, Analytical approaches to RNA profiling data for the identification of genes enriched in specific cells. *Nucleic Acids Res.* **38**, 4218–4230 (2010).
64. Z. Xie *et al.*, Gene set knowledge discovery with enrichr. *Curr Protoc* **1**, e90 (2021).
65. K. Loulier, M. Ruat, E. Traiffort, Analysis of hedgehog interacting protein in the brain and its expression in nitric oxide synthase-positive cells. *Neuroreport* **16**, 1959–1962 (2005).
66. A. D. Garcia, R. Petrova, L. Eng, A. L. Joyner, Sonic hedgehog regulates discrete populations of astrocytes in the adult mouse forebrain. *J. Neurosci.* **30**, 13597–13608 (2010).
67. R. A. Ihrie *et al.*, Persistent sonic hedgehog signaling in adult brain determines neural stem cell positional identity. *Neuron* **71**, 250–262 (2011).
68. L. A. Quina, S. Wang, L. Ng, E. E. Turner, Brn3a and Nurr1 mediate a gene regulatory pathway for habenula development. *J. Neurosci.* **29**, 14309–14322 (2009).
69. M. J. Marks *et al.*, Two pharmacologically distinct components of nicotinic receptor-mediated rubidium efflux in mouse brain require the beta2 subunit. *J. Pharmacol. Exp. Ther.* **289**, 1090–1103 (1999).
70. A. S. Vallés, F. J. Barrantes, Dysregulation of neuronal nicotinic acetylcholine receptor-cholesterol crosstalk in autism spectrum disorder. *Front. Mol. Neurosci.* **14**, 744597 (2021).
71. J. Wang *et al.*, Mediating effects of smoking and chronic obstructive pulmonary disease on the relation between the CHRNA5-A3 genetic locus and lung cancer risk. *Cancer* **116**, 3458–3462 (2010).
72. N. L. Saccone *et al.*, Multiple independent loci at chromosome 15q25.1 affect smoking quantity: A meta-analysis and comparison with lung cancer and COPD. *PLoS Genet.* **6**, e1001053 (2010).
73. T. E. Thorgeirsson *et al.*, A variant associated with nicotine dependence, lung cancer and peripheral arterial disease. *Nature* **452**, 638–642 (2008).
74. L. J. Bierut *et al.*, Variants in nicotinic receptors and risk for nicotine dependence. *Am. J. Psychiatry* **165**, 1163–1171 (2008).
75. T. E. Thorgeirsson *et al.*, A rare missense mutation in CHRNA4 associates with smoking behavior and its consequences. *Mol. Psychiatry* **21**, 594–600 (2016).
76. K. P. Jensen *et al.*, A CHRNA5 smoking risk variant decreases the aversive effects of nicotine in humans. *Neuropsychopharmacology* **40**, 2813–2821 (2015).
77. J. Z. Liu *et al.*; Wellcome Trust Case Control Consortium, Meta-analysis and imputation refines the association of 15q25 with smoking quantity. *Nat. Genet.* **42**, 436–440 (2010).
78. L. J. Bierut, Convergence of genetic findings for nicotine dependence and smoking related diseases with chromosome 15q24-25. *Trends Pharmacol. Sci.* **31**, 46–51 (2010).
79. T. Lao *et al.*, Haploinsufficiency of Hedgehog interacting protein causes increased emphysema induced by cigarette smoke through network rewiring. *Genome Med.* **7**, 12 (2015).
80. X. Zhou *et al.*, Gene expression analysis uncovers novel hedgehog interacting protein (HHIP) effects in human bronchial epithelial cells. *Genomics* **101**, 263–272 (2013).
81. E. R. E. Schmidt, R. J. Pasterkamp, The molecular mechanisms controlling morphogenesis and wiring of the habenula. *Pharmacol. Biochem. Behav.* **162**, 29–37 (2017).
82. C. Halluin *et al.*, Habenular neurogenesis in zebrafish is regulated by a hedgehog, Pax6 proneural gene cascade. *PLoS One* **11**, e0158210 (2016).
83. M. Lee *et al.*, Tcf7l2 plays crucial roles in forebrain development through regulation of thalamic and habenular neuron identity and connectivity. *Dev. Biol.* **424**, 62–76 (2017).
84. G. Brannigan, J. Hénin, R. Law, R. Eckenhoff, M. L. Klein, Embedded cholesterol in the nicotinic acetylcholine receptor. *Proc. Natl. Acad. Sci. U.S.A.* **105**, 14418–14423 (2008).
85. E. Lauwers, R. Goodchild, P. Verstreken, Membrane lipids in presynaptic function and disease. *Neuron* **90**, 11–25 (2016).
86. R. Rohatgi, L. Milenkovic, M. P. Scott, Patched1 regulates hedgehog signaling at the primary cilium. *Science* **317**, 372–376 (2007).
87. R. N. Cupédo, H. de Weerd, Tanycytes in the medial habenular nucleus of the rat. *Anat. Embryol. (Berl.)* **172**, 7–10 (1985).
88. O. Shalem *et al.*, Genome-scale CRISPR-Cas9 knockout screening in human cells. *Science* **343**, 84–87 (2014).
89. A. Dobin *et al.*, STAR: Ultrafast universal RNA-seq aligner. *Bioinformatics* **29**, 15–21 (2013).
90. S. Anders, P. T. Pyl, W. Huber, HTSeq–a Python framework to work with high-throughput sequencing data. *Bioinformatics* **31**, 166–169 (2015).
91. A. Kuryatov, J. Onksen, J. Lindstrom, Roles of accessory subunits in alpha4beta2(*) nicotinic receptors. *Mol. Pharmacol.* **74**, 132–143 (2008).
92. S.P.B. Caligiuri *et al.*, Hedgehog-interacting protein acts in the habenula to regulate nicotine intake. NCBI: GEO. https://www.ncbi.nlm.nih.gov/geo/query/acc.cgi?acc=GSE217000. Deposited 6 November 2022.